Numerical Simulations of a Gravity Wave Event over CCOPE. Part I: The Role of Geostrophic Adjustment in Mesoscale Jetlet Formation

MICHAEL L. KAPLAN, STEVEN E. KOCH, YUH-LANG LIN, RONALD P. WEGLARZ, AND ROBERT A. ROZUMALSKI

Department of Marine, Earth and Atmospheric Sciences, North Carolina State University, Raleigh, North Carolina

(Manuscript received 2 January 1996, in final form 12 August 1996)

ABSTRACT

Mesoscale model simulations are performed in order to provide insight into the complex role of jet streak adjustments in establishing an environment favorable to the generation of gravity waves on 11–12 July 1981. This wave event was observed in unprecedented detail downstream of the Rocky Mountains in Montana during the Cooperative Convective Precipitation Experiment. The high-resolution model simulations employ a variety of terrain treatments in the absence of the complicating effects of precipitation physics in order to examine the complex interactions between orography and adiabatic geostrophic adjustment processes.

Results indicate that prior to gravity wave formation, a four-stage geostrophic adjustment process modified the structure of the mid- to upper-tropospheric jet streak by creating secondary mesoscale jet streaks (jetlets) to the southeast of the polar jet streak in proximity to the gravity wave generation region (WGR). During stage I, a strong rightward-directed ageostrophic flow in the right exit region of the polar jet streak (J_1) developed over west-central Montana. This thermally indirect transverse secondary circulation resulted from inertial-advective adjustments wherein momentum was transported downstream and to the right of J_1 as air parcels decelerated through the exit region.

During stage II, a highly unbalanced jetlet (J_2) formed just northwest of the WGR in response to the inertial-advective forcing accompanying the ageostrophic circulation associated with J_1. The mass field adjusted to this ageostrophic wind field. An adiabatic cooling and warming dipole resulting from this thermally indirect secondary circulation was the cause for frontogenesis and a rightward shift in the midtropospheric pressure gradients. Since this secondary circulation associated with J_2 occurred above a dramatic vertical variation in the thermal wind, the vertical transport of potentially colder air from below was larger ahead of and to the right of J_1, thus shifting the new jetlet (J_2) well away from J_1 as the mass field adjusted to the new wind field.

Stage III was established when the new mass field, which developed in association with J_2 during stage II, set up a dynamically unbalanced circulation oriented primarily across the stream, and directly over the WGR. This new leftward-directed ageostrophic cross-stream flow (A) formed between jetlet J_2 and the original exit region of the polar jet streak J_1.

Finally, a midlevel mesoscale jetlet (J_3) is simulated to have developed in stage IV over the WGR in response to the integrated mass flux divergence associated with both the stage II and III adjustment processes. This lower-level return branch circulation to jetlet J_2 was further enhanced by velocity divergence accompanying the localized cross-stream ageostrophic wind maximum (A), which develops during stage III. The entire multistage geostrophic adjustment process required about 12 h to complete over a region encompassing approximately 400 km $\times$ 400 km.

1. Introduction

One of the most enduring problems in dynamical meteorology concerns the mechanism by which mesoscale gravity waves are generated in the atmosphere. Reviews of theories of gravity wave initiation provided by Uccellini and Koch (1987) and Koch and Dorian (1988) point to four dominant physical mechanisms that may generate gravity waves: shear instability, convection, orographic forcing, and geostrophic adjustment. Typically, however, either observations have been inadequate, or numerical experiments too limited by computational resources and numerics to thoroughly investigate the dynamical mechanisms for wave genesis.

The recent study by Powers and Reed (1993) of the large-amplitude gravity waves accompanying the 14–15 December 1987 midwest cyclone is a major advance in the ability to address the issue of mesoscale gravity wave generation by use of mesoscale model simulation results. However, one fundamental limitation with that study (which proposes convection/wave-CISK as the wave generation/maintenance mechanism) lies in the nonexistence of mesoscale rawinsonde information both downstream and within the wave generation region (WGR) against which simulation results could be verified. Furthermore, questions can be raised concerning the adequacy of the horizontal resolution of the mesoscale model employed, the timing of the initialization,

Corresponding author address: Prof. Yuh-Lang Lin, Department of Marine, Earth and Atmospheric Sciences, Campus Box 8208, North Carolina State University, Raleigh, NC 27695-8208.
E-mail: yl_lin@ncsu.edu

as well as the surface datasets utilized in the wave analyses of the same case study as presented in Schneider (1990). Most importantly, the strong emphasis on wave-CISK can be called into question, because removal of moisture from the mesoscale model to examine the importance of convection also affects the degree of synoptic-scale dynamical balance through its effect on the magnitude and wavelength of the upper-tropospheric trough–ridge system. This exerts a major control on the behavior of air parcels exiting the jet streak, in geostrophic adjustment processes, and in inertia–gravity wave generation.

Other modeling studies have produced convectively forced gravity waves, though with a dearth of observations against which to verify the results. For example, in a two-dimensional model simulation, Tripoli and Cotton (1989) compare simulated internal gravity waves, launched by differential surface sensible heat fluxes between an elevated plateau and adjacent plains region, to satellite observations of convection accompanying these waves. However, no detailed surface analyses of the observed wave characteristics were attempted in an effort to compare the simulated waves to observations. Likewise, Zhang and Fritsch (1988) and Schmidt and Cotton (1990) lack the detailed observational mesoscale dataset needed to compare simulated and observed waves and, hence, diagnose unambiguously the physical mechanism(s) responsible for wave genesis.

A series of papers by Koch and Golus (1988), Koch et al. (1988), Koch and Dorian (1988), and Koch et al. (1993) together represent an unprecedented study of mesoscale gravity waves. Their studies utilized special observations taken during the Cooperative Convective Precipitation Experiment (CCOPE) on 11–12 July 1981. Mesoscale surface and rawinsonde observations, high-resolution radar and satellite data, multiple Doppler radar wind analysis and thermodynamic retrievals, and the predictions from linear stability theory were synthesized. Cross spectral analysis revealed that the waves were bimodal (displaying wavelengths of 160 and 70 km) and bipartite (consisting of two wave episodes).

Efforts were made in these CCOPE studies to determine the role played by geostrophic adjustment, wave-CISK, and shear instability in generating the observed gravity waves. The results strongly supported geostrophic adjustment as the most likely wave generation mechanism. In particular, Koch and Dorian (1988) showed that ''unbalanced flow conditions'' at the 300-hPa level, as diagnosed from the synoptic and special rawinsonde data, developed shortly before the initiation of internal gravity waves was observed in nature. Unbalanced flow was defined as high Lagrangian Rossby number (Ro $>$ 0.5) in the presence of cross-contour ageostrophic flow directed in a sense that is inconsistent with the predictions from quasi- and semigeostrophic theory; namely, a thermally *direct* circulation in the *exit* region of the geostrophic jet. The linear theory and Doppler radar comparisons made by Koch et al. (1993) indicated the importance of wave overreflection and critical level processes in maintaining wave coherence. Convection was ruled out as a wave generation mechanism, since many of the waves first appeared over the mountains of western Montana without any accompanying deep convection, and the quantitative predictions from wave-CISK theory compared poorly with the observed wave characteristics. Nevertheless, once the gravity waves triggered thunderstorms, strong convective feedback effects were observed to amplify the wave pressure field and to locally alter the wave energetics, thus suggesting that wave-CISK was qualitatively still a factor in wave *amplification/maintenance.*

Unfortunately, the CCOPE upper-air dataset was confined to the region over the gravity wave observational network, which was downstream of the WGR. A comprehensive numerical modeling investigation needs to be compared to the detailed observational analyses for this case. A favorable comparison would indicate high confidence in a model-derived analysis of the dynamics of wave generation unachievable with either mesoscale observations or numerical model results separately. This analysis would have the unique combination of model-simulated mesoscale processes, mesoscale rawinsonde and radar data, and detailed mesonet surface analyses for comparison to observed wave development and propagation characteristics. The use of a mesoscale numerical model to diagnose the mechanism(s) for the generation, evolution, and maintenance of the observed dual episode of CCOPE mesoscale gravity waves represents the purpose of this and subsequent papers in this series.

In this first paper (Part I), we endeavor to diagnose the role of upper- and midlevel *mesoscale* jet streaks (jetlets) in organizing the precursor mesoscale conditions for the first of the two gravity wave episodes observed by Koch and Golus (1988). Numerical simulations are conducted in an effort to define the geostrophic adjustment processes associated with the mid- to upper-level jet streak. The results indicate that the generation of a 600–700-hPa mesoscale jet streak arising from a complex and relatively fast sequence of geostrophic adjustment processes is critical to the formation of mesoscale perturbations over the WGR that display characteristics quite similar in most respects to the observed gravity waves, except that they propagate very slowly. Although geostrophic adjustment processes associated with an unbalanced upper-level jet appear to occur in a manner similar to that diagnosed by Koch and Dorian (1988), the model indicates that middle-lower tropospheric mass adjustments (an isallobaric response) associated with the interaction of a mesoscale jetlet and orography are required for the generation of the wave-like perturbations. We do not make an attempt to assess the role of the critical level, wave ducting, or wave-CISK processes in gravity wave generation in this first paper. In fact, we purposely prevent latent heat release

TABLE 1. Composition of the GMASS mesoscale model used in this study.

Numerics
• 3D primitive equations for *u, v, T, q,* and *p*
• Terrain-following σ–*p* vertical coordinate
• Arakawa ''A'' grid on a polar stereographic map image plane
• Fourth-order accurate horizontal spatial differencing
• Split-explicit time integration employing the Adams–Bashforth and Messinger schemes
• Fourth-order biharmonic diffusion operator
• One-way interactive grid nesting
• Time-dependent lateral boundary conditions from NMC analyses
• Sponge-type upper boundary condition
Initialization
• LFM analysis of 10 mandatory pressure levels as first guess
• Reanalysis using Barnes scheme applied to significant level and surface data
• Interpolation to finer mesh using cubic splines under tension
• ''Static initialization'' removes integrated mass divergence (eliminates external gravity wave, but not internal waves)
PBL formulation
• Blackadar high resolution PBL scheme (Zhang and Anthes 1982)
• Force–restore surface energy budget over land
Moisture physics (although not used in present paper, will be discussed in future papers on the CCOPE simulations)
• Grid-scale condensation based on layer supersaturation
• Explicit liquid water and ice continuity equations
• Condensate can evaporate in unsaturated layers
• Fritsch–Chappell (1980) and Molinari (1982) cumulus parameterization schemes
Radiation
• Radiation is considered only in the surface energy budget

from occurring, in order to focus on the background jet dynamical processes.

Section 2 describes the numerical model and the details of the simulation experiments. We discuss the observed synoptic-scale environment preceding the generation of internal gravity waves in section 3. The synoptic-scale simulation, produced by the model with degraded horizontal resolution, is compared to the available upper-air observations in section 4. This is done in order to build confidence in the mesoscale simulation results as well as to improve our understanding of the significance of the observed synoptic-scale processes outlined in section 3. The analysis of the evolution of the primary mid- to upper-tropospheric jet streak into multiple ageostrophic mesoscale jetlets and their relationship to frontogenesis is presented in section 5. Sensitivity of the simulated set of geostrophic adjustment processes to a spectrum of terrain configurations will also be addressed. Section 6 concludes with a discussion and summary of the major results.

2. Numerical model and experiments

The numerical model used in the experiments is the GMASS (Goddard Mesoscale Atmospheric Simulation System) model (e.g., Manobianco et al. 1994). This is a modified version of the MASS model, which has been employed in a wide variety of simulation studies (e.g., Kaplan et al. 1982; Koch 1985; Koch et al. 1985; Zack and Kaplan 1987; Whitaker et al. 1988; Manobianco et al. 1991, 1992; Kaplan and Karyampudi 1992a,b). Table 1 describes the details of the model version used in this study. This hydrostatic model employs a sigma vertical coordinate system, a one-way nested grid with sponge/open (Perkey–Kreitzberg/Orlanski) lateral boundary conditions, a Blackadar planetary boundary layer formulation with a complete surface energy budget, and an additional artificial sponge layer whose Rayleigh friction coefficient increases with height within the model stratosphere for effective gravity wave absorption. For the experiments to be described in this paper, *all condensational heating was suppressed,* so that the role of physics other than latent heat release in the geostrophic adjustment process could be identified. Soil moisture was set to a uniformly low value, consistent with the hypothesis that physical processes other than condensational heating dominate the development of the precursor midlevel mesoscale jetlet over the WGR. The role of moisture physics on wave generation and evolution will be discussed in a separate paper. Although sensible heat fluxes do occur in all simulations reported in the present paper, the role of boundary layer processes will be reported in Part II due to their highly complex interactions with the background geostrophic adjustment processes discussed herein.

The coarse- and nested-grid regions over which the model was integrated, as well as key observing station locators are depicted in Fig. 1. The nested grid was centered just downstream from the WGR identified by Koch and Dorian (1988), which is located over the region bordering Montana, Wyoming, and Idaho (Fig. 2). This places the region between the WGR and CCOPE

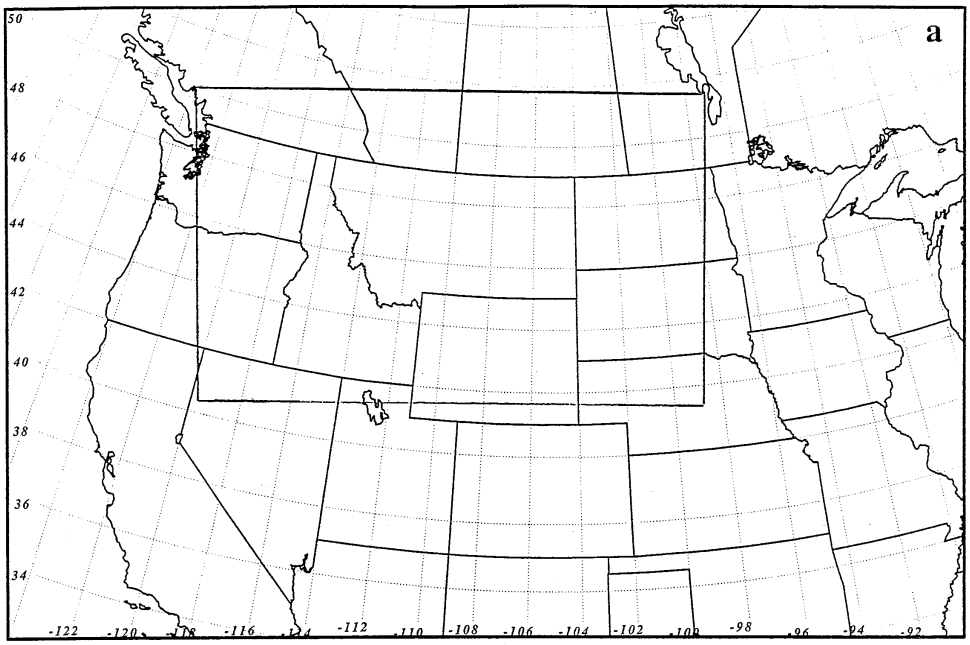

FIG. 1. (a) Large (small) box represents the region of integration for 16- (8-) km coarse-(nested) resolution GMASS simulations. (b) Location of rawinsonde and hourly reporting stations. Upper-air stations are indicated in bold script and include Boise, Idaho (BOI), Lander, Wyoming (LND), Great Falls, Montana (GTF), Glasgow, Montana (GGW), and Rapid City, South Dakota (RAP).

(Figs. 2b,c) in the middle of the nested-grid computational domain. A matrix of 223 × 146 × 30 grid points was employed for both the coarse (16 km) and nested (8 km) grid simulations. These horizontal resolutions, true at 90°N, imply even finer resolution over the region of interest centered at approximately 47.5°N. The specific horizontal resolutions were selected to fully resolve, with a minimum of 10 grid points, the primary ($\lambda \sim 160$ km) and secondary ($\lambda \sim 70$ km) gravity wavelengths observed by Koch and Golus (1988) without violating the hydrostatic assumption. Thirty vertical levels were uniformly spaced between the planetary boundary layer and the model top, which is located at 100 hPa. Hydrostatic consistency was maintained by choosing a horizontal grid interval Δx and the vertical separation between sigma-p surfaces $\Delta\sigma$ such that $\Delta\sigma/\Delta x < \Delta h/\Delta x$ (the maximum terrain slope).

Three different terrain geometries were used in the

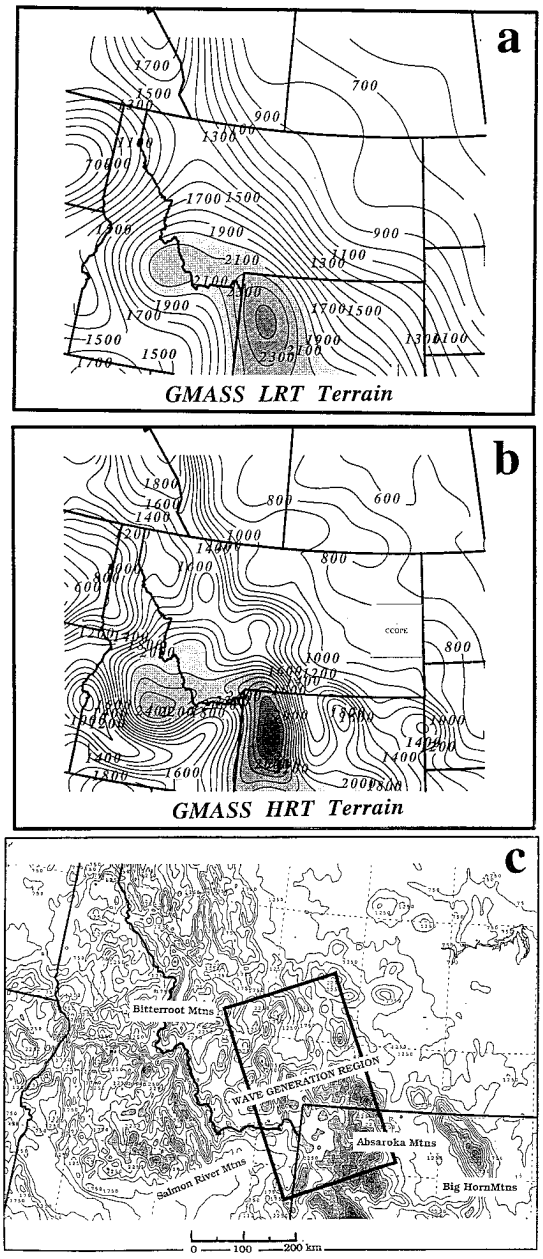

FIG. 2. (a) Low-resolution terrain (LRT) simulation, (b) high-resolution terrain (HRT) simulation, and (c) observed (8 km) terrain databases (m). The rectangle in panel (b) represents the CCOPE mesonet region, whereas that in (c) represents the wave generation region (WGR) after Koch and Golus (1988). Terrain heights greater than or equal to 2 km are shaded.

four simulations to be described in this first paper (Table 2). Experiments 1 and 2 employ a uniform terrain wherein the northern Rockies are effectively removed and replaced by a flat, rigid plate with a horizontally homogeneous surface value of 1500 m MSL. This terrain is used for the ''uniform terrain'' (UT) mesoscale and ''quasigeostrophic'' (QG) synoptic-scale simulations, which employ grid resolutions of 16 and 125 km,

TABLE 2. Summary of the seven model simulation experiments.

Simulation	Horizontal resolution[a] (km)	Number of vertical levels	Terrain type[b]	Model physics[c]
QG	125	30	Uniform	PBL/No LH
UT	16/8	30	Uniform	PBL/No LH
LRT	16/8	30	LFM	PBL/No LH
HRT	16/8	30	High	PBL/No LH

[a] N/M—Ratio of coarse/nested fine grid horizontal mesh sizes; QG contains only the coarse grid.

[b] Uniform terrain is horizontally homogeneous 1500-m high terrain. LFM terrain is that used in the NWS LFM II model. High-resolution terrain is derived from an 8-km-resolution terrain database.

[c] PBL refers to use of full PBL physics. No LH means that stratiform and convective latent heating is totally suppressed although atmosphere is moist.

respectively. Experiment 3 employs a National Weather Service (NWS) Limited-Area Fine-Mesh (LFM) model terrain (Fig. 2a), and is referred to hereafter as the mesoscale low-resolution terrain (LRT) simulation. Finally, experiment 4 employs a high-resolution terrain (HRT), which was derived from an 8-km-resolution database, but highly smoothed in order to prevent any terrain instability according to Phillips' (1957) criteria (Fig. 2c shows the original 8-km-resolution terrain field). Notice that the WGR is located over the Absaroka and Bitterroot mountain region of southwestern Montana, southeastern Idaho, and northwestern Wyoming. Four of the seven numerical experiments described in Table 2 will be discussed in this paper. These four specific experiments were performed in an effort to gauge the effect of orographic forcing as well as model resolution on the initiation of the observed gravity waves. The numerical experiments to be discussed herein consist of the 125-km-resolution QG simulation, the 16-km ''coarse mesh'' UT simulation, and the 8-km ''fine mesh'' LRT and HRT terrain simulations. Each model run includes diabatic planetary boundary layer processes. Results from these four simulations (to be compared later) show that the basic jet streak geostrophic adjustment processes occur independent of terrain features, but that gravity wave development occurs only in the presence of topography. Features of the simulated gravity waves become similar to the observed waves as the terrain realism is improved.

The coarse mesh simulations were initialized at 0000 UTC 11 July 1981 and forecasts were produced for the 30-h period ending at 0600 UTC 12 July 1981. This period includes both episodes of observed gravity waves as well as the initiation of the mesoscale convective system (MCS) over eastern Montana as described by Koch et al. (1988). The initial conditions for each coarse mesh simulation were derived from the LFM analyses and North American rawinsonde and hourly surface data. Lateral boundary conditions were prescribed from LFM 6-h forecast data as well as 12-h observations. The

nested-grid simulation was initialized at 0900 UTC 11 July 1981 and integrated through 0600 UTC 12 July 1981. This time for the initialization of the nested-grid simulations was chosen for two reasons: (a) it allowed sufficient time for the coarse-grid forecast to evolve into a quasi-balanced state not contaminated by inertia–gravity waves resulting from initialization imbalances before starting up the finer grid forecast, and (b) the first episode of the observed gravity waves develops over the WGR on or about 1100 UTC 11 July 1981. The initial conditions for the nested-grid simulations were derived from cubic spline interpolated coarse mesh fields, and the one-way lateral boundary conditions needed for the nested-grid simulations were derived from interpolated hourly coarse mesh simulated fields.

3. Early observed synoptic conditions

a. Mid- to upper-tropospheric rawinsonde data

Figure 3 displays objective analyses of the NWS rawinsonde data at 850, 700, 500, and 300 hPa for 0000 UTC 11 July 1981. A broad ridge of high pressure over the Plains states and a cutoff low pressure area over western Washington are evident in these synoptic-scale analyses. Also apparent are the following important features:

1) A thermal ridge at the 700- and 850-hPa levels from eastern Wyoming to southern Saskatchewan, which acts to quasigeostrophically enhance the synoptic-scale ridge in the upper-tropospheric height field.
2) The 500–300-hPa-level polar jet streak extending from just west of the California coast to the northern Rockies, with an exit region over eastern Idaho and western Montana.
3) A short-wave trough in the 700–300-hPa height fields extending from eastern Washington, across Idaho, and into northern Utah.
4) A midtropospheric front that is most pronounced over Idaho at 500 hPa.
5) A weak low-level jet at 700 hPa over eastern Washington and Oregon.
6) A strong midtropospheric lapse rate over the intermountain region, including the region between the WGR and CCOPE. Very warm air at 700 hPa over the southeastern part of the WGR lies underneath rather cold air at 500 hPa. Thus, three very different vertical lapse rates occur between 850 and 300 hPa, that is, nearly dry adiabatic sandwiched in between two stable layers.

Depicted in Fig. 4 is the corresponding set of analyses 12 h later. While there are no major changes in the synoptic-scale flow pattern, the shortwave trough has propagated northeastward toward western Montana (as evidenced by the height falls and enhanced height gradient caused by cooling at 500 hPa northwest of the WGR), whereas the exit region of the jet streak at 300 hPa is still located between central Idaho and southwestern Montana. Additionally, substantial cooling at the 850-hPa level has contributed to a reduction in the amplitude of the mid- to upper-tropospheric ridge over the elevated terrain from western Wyoming to southwestern Canada. This analysis cannot resolve whether mesoscale temperature and wind perturbations are superimposed upon the synoptic-scale tendencies.

An important inference to be discerned from the 1200 UTC 500-hPa fields depicted in Figs. 4 and 5 is evidence for weak cooling over central Idaho and central Montana during the preceding 12-h period. These midtropospheric temperature changes could be due to any combination of adiabatic ascent, cold advection (unlikely since only weak warm advection is noticeable), or to diurnal cooling often observed in rawinsonde data over mountainous regions. The evidence suggests the importance of adiabatic vertical motions in causing the cooling pattern. A cross-stream wind component in the exit region directed toward the cyclonic side of the polar jet streak is seen over eastern Washington and northwestern Montana at 1200 UTC, and over central Idaho 12 h earlier. Also notice the rightward component directed to the jet streak's anticyclonic side in eastern Montana and Wyoming at both times. The thermally direct and indirect transverse circulations implied by this combination of cross-contour flow could produce cooling along the jet axis of a few degrees (associated with the rising branch of the mutually interacting circulations) and warming both to the left and right of the jet axis (associated with the two descending branches) as observed at 500 hPa (Fig. 5).

Similar temperature and height changes occur at the 700-hPa level. This differential height fall pattern is also consistent with the 1200 UTC occurrence of a weak 700-hPa wind maximum. It will be shown from the model simulations that this midlevel jet develops directly southeast of the midtropospheric region of observed cooling and is in close proximity to the WGR (located over the borders of Montana, Idaho, and Wyoming). The 850-hPa and surface winds over the elevated terrain of southeastern Idaho and western Wyoming reflect this increasing southwesterly flow regime.

b. Satellite observations

Figure 6 depicts infrared satellite imagery at 1200 UTC 11 July 1981 over the northern Rocky Mountain region. A striking feature in this imagery is the appearance of two cirrus streaks or plumes. The first streak extends from southeastern Oregon to northern Montana, and occurs on the cyclonic side of the primary polar jet streak, while the second streak is located approximately 250 km to its southeast. The first gravity wave event observed by Koch and Golus (1988) forms within the second cirrus plume over the WGR. A plausible intepretation of this imagery is that these cirrus streaks could indicate that a secondary upper-level jet streak

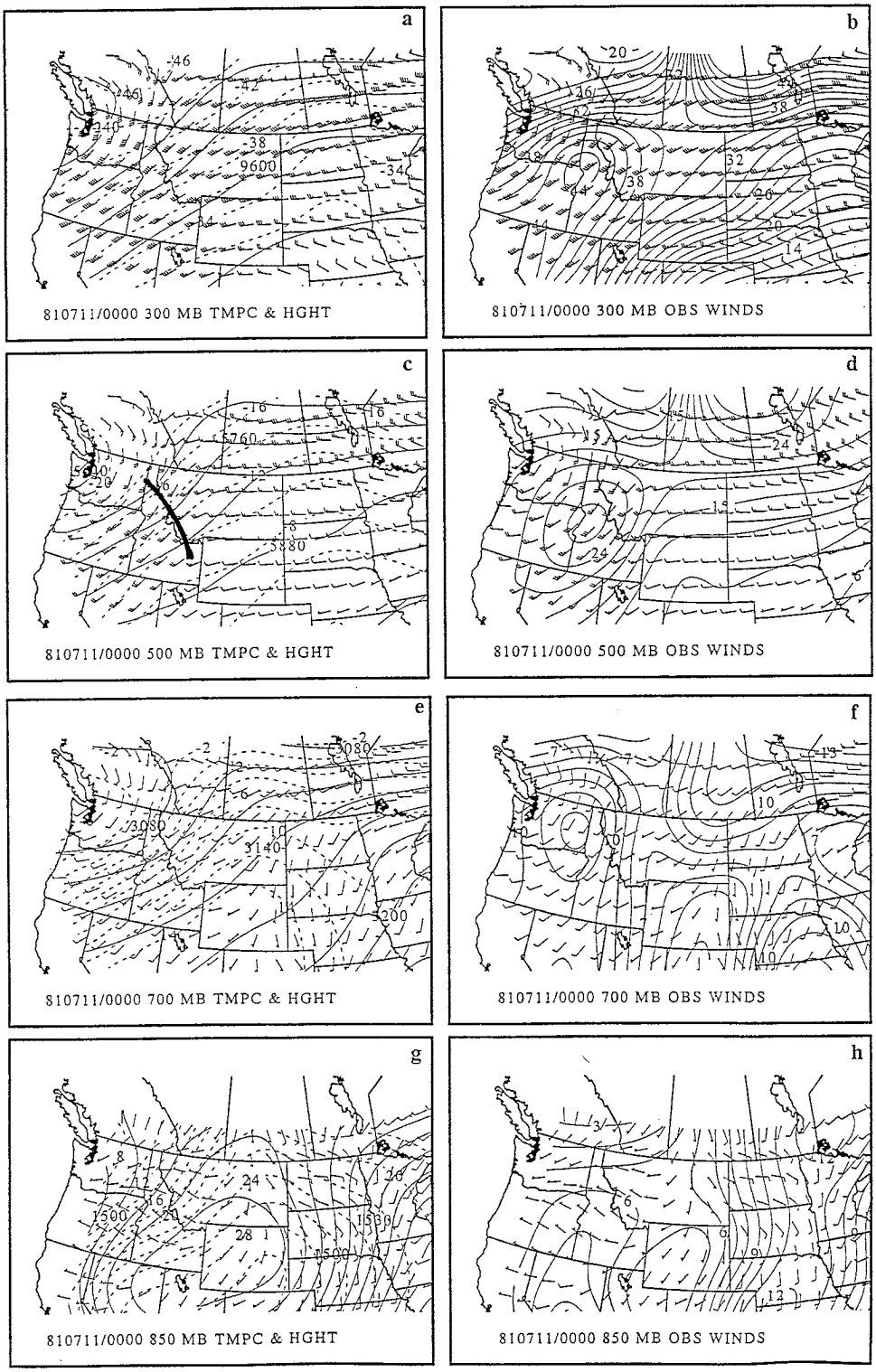

FIG. 3. Barnes objective analyses of rawinsonde data at 0000 UTC 11 July 1981 (a) isotherms (°C, dashed lines), geopotential height (m, solid lines), and wind vectors at 300 hPa; (b) isotachs (m s^{-1}) and wind vectors at 300 hPa; (c),(d) same as in (a),(b) except at 500 hPa; (e),(f) same as in (a),(b) except at 700 hPa; and (g),(h) same as in (a),(b) except at 850 hPa. Position of short-wave trough at 500 hPa is depicted by thick, solid line.

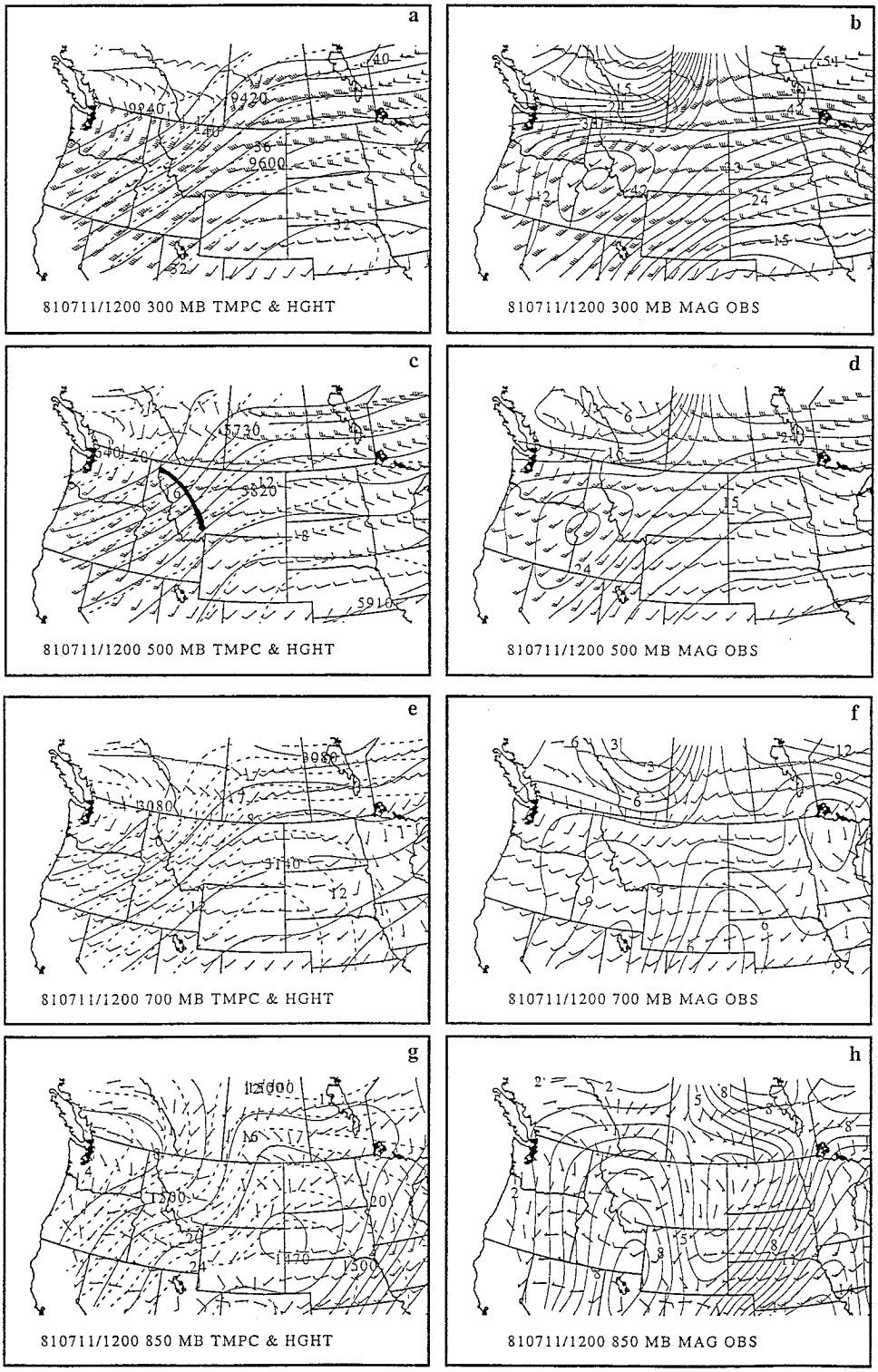
a
9420
9600
9780
9940
10100
10260
10420
10580
10740
10900
11060
11220
11380
11540
11700
11860
12020
12180
12340
12500
12660
12820
12980
13140
13300
13460
13620
13780
13940
14100
14260
14420
14580
14740
14900
15060
15220
15380
15540
15700
15860
16020

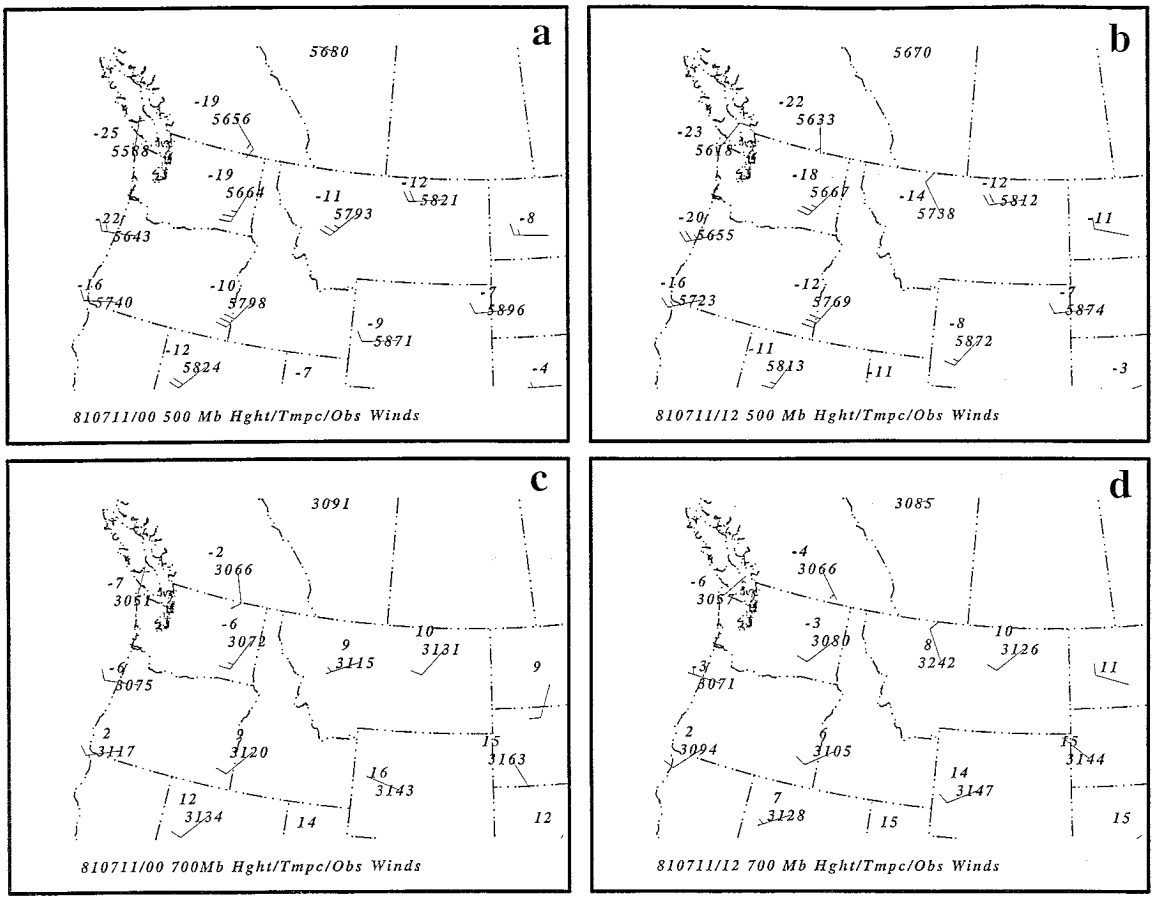

FIG. 5. Synoptic rawinsonde observations at 0000 UTC 11 July 1981 and 1200 UTC 11 July 1981 of geopotential height (m), temperature (°C), and wind (m s^{-1}) at (a),(b) 500 hPa, and (c),(d) 700 hPa. Long wind barbs represent 10 m s^{-1} and short barbs 5 m s^{-1}.

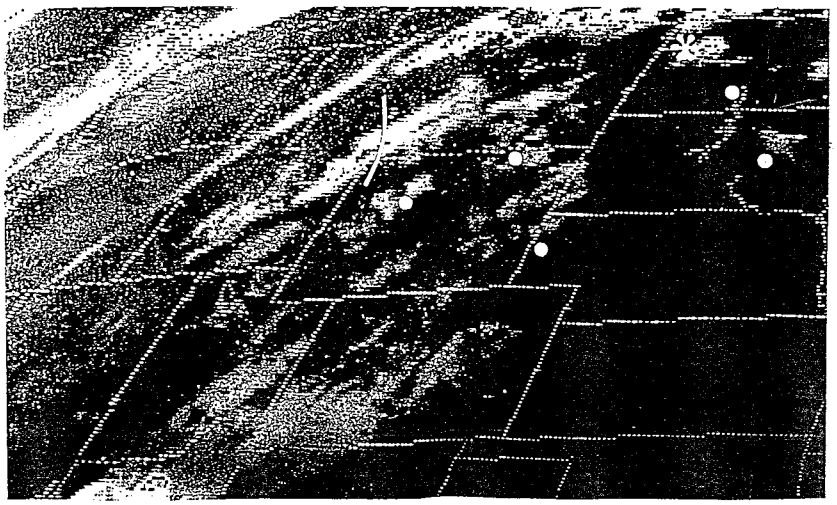

FIG. 6. Infrared satellite imagery over the northwestern United States valid at 1200 UTC 11 July 1981. The dots represent pressure pulses detected in synoptic barograph traces, but these have no spatiotemporal coherence and do not represent the gravity waves. The white arc depicts the first detected wave crest, and is associated with a cloud streak (after Koch et al. 1988).

develops by 1200 UTC with its right exit region passing over the WGR. It will be shown later that the GMASS model develops such a jet system at this time over this region. An alternative explanation for the cloud streaks is also considered. Durran and Weber (1988) have shown that a horizontal confluence zone and moisture advection on the anticyclonic side of a jet streak can produce cirriform cloud streaks similar to those arising from adiabatic cooling accompanying ascending motions on the cyclonic side of the jet. Confluence and moisture advection patterns in the present case are more consistent with the location of the secondary jet streak, whereas the cooling pattern is more indicative of the location of the primary jet streak located to the northwest (Fig. 4). An interesting comparison between Figs. 4e and 6 reveals that at 1200 UTC the second (southeastern) cirrus streak is located along the northwestern periphery of the very warm (>10°C) air mass over the intermountain region at 700 hPa.

c. Summary of synoptic observations

The rawinsonde observations indicate that cross-stream ageostrophic flow within the mid- to upper-troposphere jet exit region accompanying a short-wave disturbance, the alongstream cirrus streaks, and mid- to upper-tropospheric temperature and height falls, together represent the most significant changes in the region surrounding the WGR during the 0000–1200 UTC 11 July 1981 time period. While these changes are not dramatic, they suggest a region of cooling just north and west of the WGR, with the opposite pattern over Wyoming. Evidence has been presented that such cooling is not just the result of standard diurnal forcing, but rather reflects a mass adjustment consistent with the ageostrophic winds observed within the exit region of the upper-level jet streak. This mass adjustment requires a region of ascent surrounded on both sides by regions of descent, which is to say that a thermally direct circulation over northern Idaho and northwestern Montana is flanked by a thermally indirect circulation centered near the WGR.

The developing cross-stream ageostrophic wind pattern suggested above was also computed in the rawinsonde analysis at 1200 UTC by Koch and Dorian (1988). As shown in Fig. 7b, ageostrophic flow is directed toward the cyclonic side of the jet over western Idaho, and to the anticyclonic side over most of Wyoming and eastern Montana. They suggested that since the sense of the leftward-directed circulation was opposite to that predicted for the exit region of a straight jet steak from quasi- or semigeostrophic theory, which was even more apparent 12 h later, that the jet exit region was becoming increasingly unbalanced during this time period. Various measures of the Rossby number indicated that the greatest likelihood of unbalanced dynamics was over western Montana and northern Idaho, which is nearly the same region that the GMASS model produces strong ageostrophy (shown later). Notice that the geostrophic wind maximum (Fig. 7a) is located over southeastern Oregon, upstream of the jet streak over eastern Idaho (Fig. 4b). Koch and Dorian (1988) argue that this displacement between the actual and geostrophic jets is the real cause for the ageostrophy being of an unbalanced sense, since in this region $\mathbf{V}\cdot\nabla\mathbf{V} \neq \mathbf{V}\cdot\nabla\mathbf{V}_g$, which is inconsistent with the semigeostrophic set of equations. The apparently unbalanced ageostrophic flow lies just northwest of the strong vertical variation of lapse rates mentioned above.

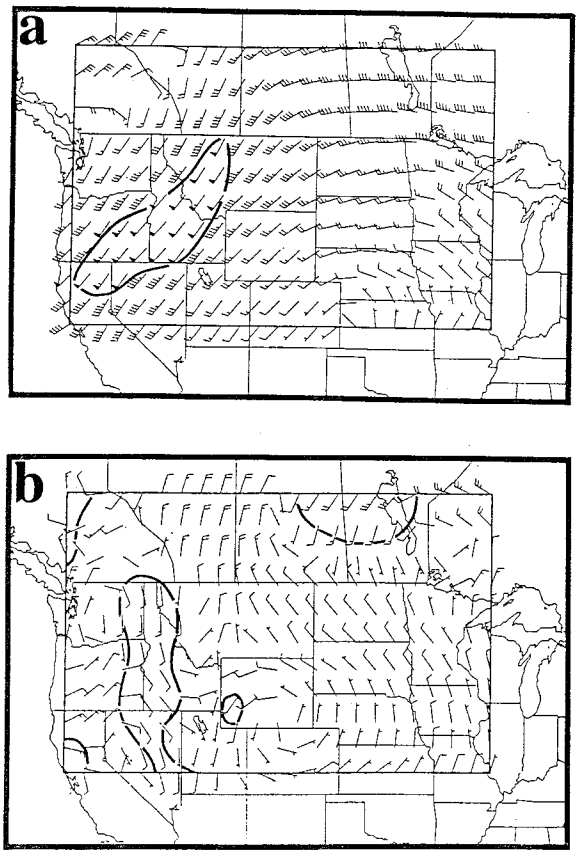

FIG. 7. Indications of unbalanced flow at 1200 UTC 11 July 1981 based on objective analysis of synoptic and CCOPE mesonet rawinsonde data. (a) Geostrophic wind vectors (m s^{-1}) and 50 m s^{-1} isotach and (b) ageostrophic wind vectors (m s^{-1}) and isotach of ageostrophic winds in excess of 10 m s^{-1} directed toward lower heights (after Koch and Dorian 1988).

4. Comparison of synoptic-scale QG simulation to standard observations

In an effort to determine the ability of the numerical model to properly define the synoptic-scale circulations prior to the development of simulated mesoscale circulations, a coarse (125 km) mesh simulation (QG) was first performed (Table 2). This simulation is important for demonstrating that the model could accurately simulate the quasigeostrophic circulations implied in the

observations as outlined in the previous section, prior to analyzing the numerical results of the much more complex mesoscale processes.

The 12-h temperature and height change fields at 500 hPa and 700 hPa from the QG and UT model simulations are depicted in Fig. 8. The observations (Fig. 5) and the QG simulation both indicate 500-hPa cooling extending from western North Dakota, across most of Montana, to southern Idaho, and warming over Washington and Oregon. The simulated temperature change pattern is qualitatively consistent with the rawinsonde observed changes for the period 0000–1200 UTC 11 July 1981, with the exception that the QG simulation underestimates the slight (1°C) warming that actually occurs over Wyoming and exaggerates the warming over the Pacific Northwest. The QG cooling and associated height fall patterns are consistent with weak positive vorticity advection occurring within the exit region of the jet streak, as inferred from the observations depicted in Figs. 3 and 4. These simulated QG temperature changes add credence to the hypothesis that the observed 500-hPa changes are dynamically forced and not merely the result of standard diurnal changes. The more detailed patterns in the UT simulation (Figs. 8e–h) agree even better with the regional observations, since at 500 hPa slight warming occurs over western Wyoming and the degree of warming over the Pacific Northwest is much more realistic. Furthermore, at 700 hPa the model captures the dramatic cooling across southern Oregon and northern Nevada, as well as the strong warming over eastern Washington.

The QG simulated temperature changes are also qualitatively consistent with the adiabatic warming and cooling patterns produced by the QG vertical motions, which are shown halfway through the forecast in Fig. 9. Persistent rising motion appears within the region of 12-h cooling, and sinking motions flank the regions of rising motion; in fact, the magnitude of lifting over central Montana is double the magnitude of descent over Wyoming, consistent with the prediction of strongest cooling (3°C) over Montana. The northwest–southeast-oriented temperature gradient in this region would be enhanced by such vertical circulations. We hypothesize from these temperature and vertical velocity patterns that the observed temperature and height changes (Figs. 3 and 4) are produced by two transverse circulation cells within the exit region of the polar jet streak, as also suggested by the observations discussed earlier.

It is quite important that the 500-hPa ascent and cooling patterns are rightward-shifted relative to a classical thermally indirect secondary circulation. According to Fig. 9, subsidence occurs in association with the leftward-directed cross-contour flow at 500 and 300 hPa over northeastern Washington, southern British Columbia, and Alberta. Southeast of this thermally direct circulation is a rightward-shifted thermally indirect circulation centered near the WGR and an associated rightward-directed cross-contour flow over Wyoming. The rising branch of the thermally indirect circulation occurs over central Montana and the sinking branch is over southern Wyoming.

This simulated transverse circulation agrees in general with the observational analyses of Koch and Dorian (1988), who found convergent ageostrophic flow on the cyclonic side of the jet where GMASS simulates subsidence and divergent ageostrophic flow over central and eastern Montana where there is simulated rising motion (Fig. 7b). This kind of dual-celled circulation in the jet exit region is consistent with the balanced dynamics of a straight jet streak in which warm advection occurs in the presence of shear deformation (Keyser and Shapiro 1986). Such a flow pattern is clearly present here. The leftward-directed component in the jet exit region was referred to as ''unbalanced'' by Koch and Dorian (1988), because they did not stress the compensatory effects of thermal advection; nonetheless, the observations suggest advection effects to be rather weak.

The inferred existence of the rightward-shifted thermally indirect circulation over the WGR in the QG simulation and in the observations is bolstered by the appearance of the 700-hPa height and wind fields. Note the occurrence of a weak (10 m s^{-1}) 700-hPa wind maximum just southwest of the WGR in the QG simulated fields by 1200 UTC (Fig. 9e). This feature is consistent with the observations (Fig. 4). Such behavior is indicative of a lower-tropospheric isallobaric component of the indirect circulation in a jet streak exit region (e.g., Uccellini and Johnson 1979). Support for this conjecture is offered in Fig. 9f, which shows a vertical motion consistent with forcing by the isallobaric component of the 700-hPa jet. More in-depth discussion of these processes is presented later.

In summary, the QG simulation predicts mass and wind adjustments similar to those inferred from the synoptic-scale observations. This sequence of adjustments is also predicted by the UT mesoscale simulation (as will be shown). The QG simulation reinforces the likelihood that, prior to gravity wave generation, there existed:

- a well-developed rightward-shifted thermally indirect circulation within the right exit region of the mid- to upper-tropospheric jet streak over the WGR.
- a coupled lower branch return circulation manifested as a 700-hPa southwesterly jet immediately upstream of the WGR.
- a thermally direct circulation located to the northwest of the rightward-shifted thermally indirect circulation.

5. Diagnoses of simulated ageostrophic jetlet formation resulting from geostrophic adjustment processes

In this section we will analyze the three high resolution nested-grid simulations to relate a complex set of adjustments and their role in the initiation of mesoscale

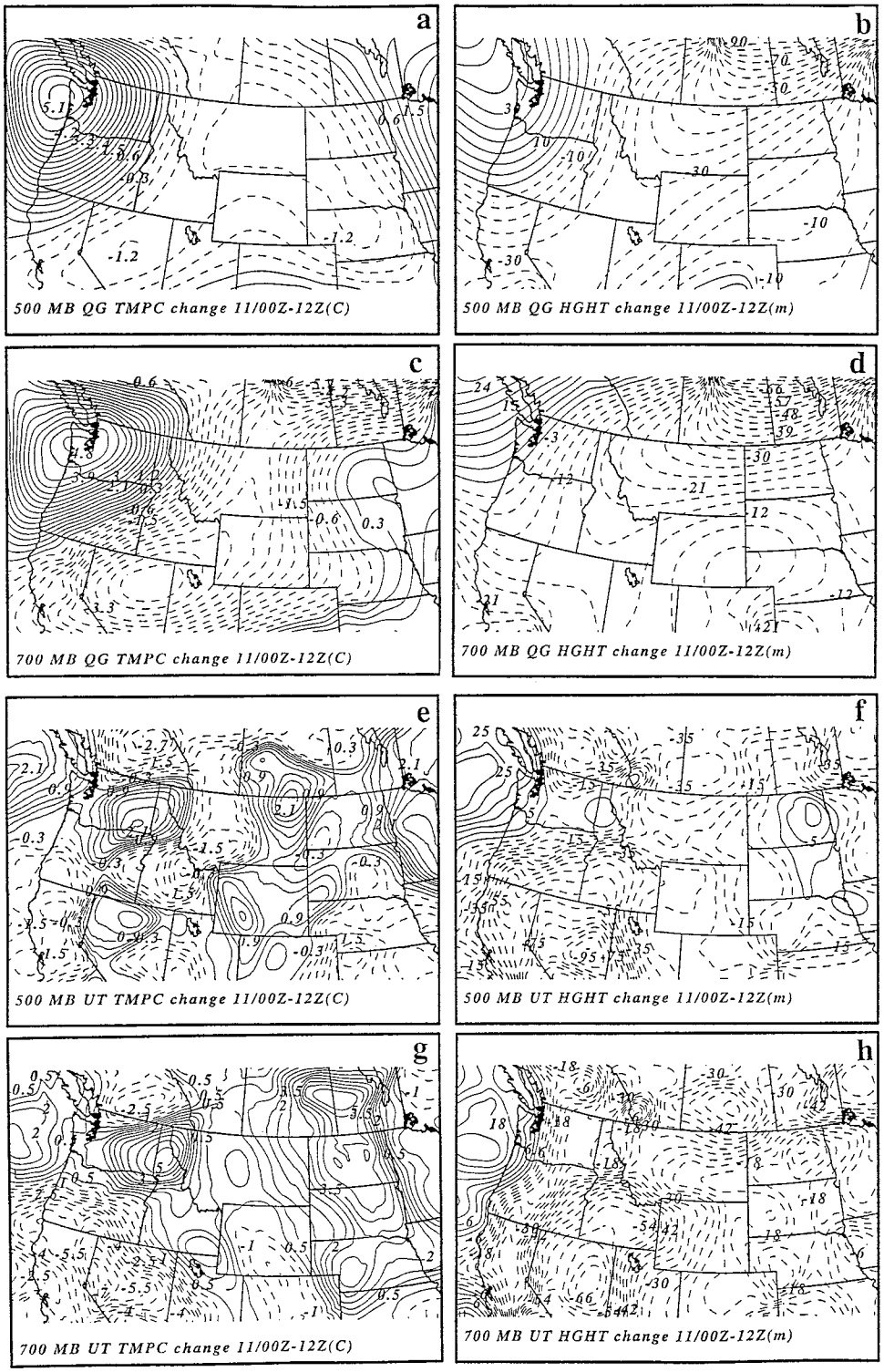

FIG. 8. The 125-km horizontal resolution synoptic-scale (QG) simulation (a)–(d) and coarse mesh (16 km) UT simulation (e)–(h) of 12-h temperature (°C) and height (m) changes at 500 and 700 hPa.

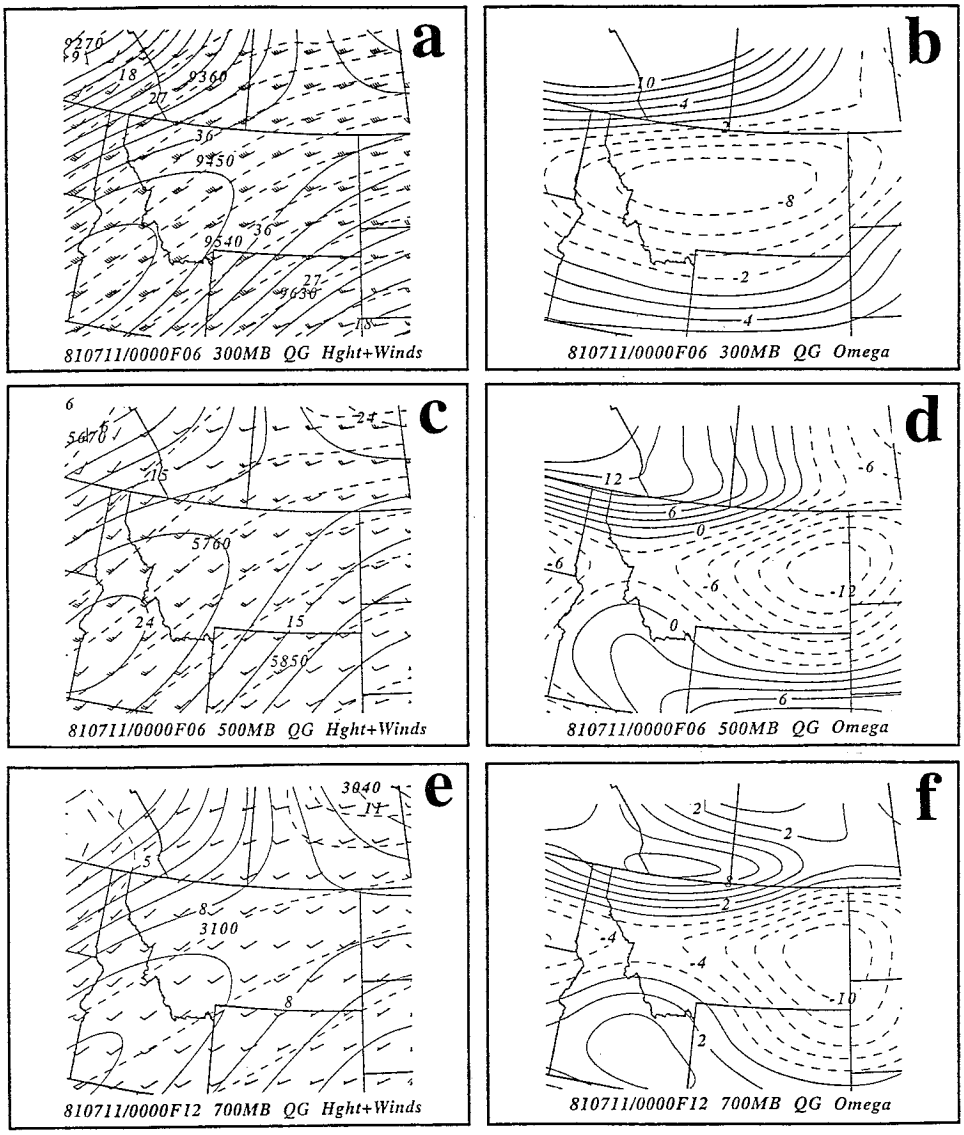

FIG. 9. Synoptic-scale (QG) simulation of wind vectors, isotachs (m s^{-1}, solid), and height fields (m, dashed) at (a) 300 hPa and (c) 500 hPa, and vertical motion (μb s^{-1}, rising—dashed, sinking—solid) at (b) 300 hPa and (d) 500 hPa valid at 0600 UTC 11 July 1981. Panels (e) and (f) show the corresponding 700-hPa simulation fields valid at 1200 UTC 11 July 1981.

mass/momentum perturbations over the WGR. We will define a four-stage geostrophic adjustment process that produces a favorable environment for the initiation of inertia-gravity waves. The key outcome of this process is the creation of a mesoscale ageostrophic jetlet in the 500–700-hPa layer over the WGR. In an effort to emphasize the geostrophic adjustment processes that occur independent of terrain forcing, we will focus on the UT mesoscale simulation. We will then compare the UT simulation results to the LRT and HRT simulations to address the following questions:

1) How does geostrophic adjustment organize the midlevel mesoscale jetlet?
2) Does this jetlet form as a result of predominantly adiabatic *non*orographic processes?
3) Are mesoscale mass/momentum perturbations excited in the absence of terrain-induced mass perturbations?
4) Is the midlevel jetlet collocated in space and time with the generation of simulated and/or observed internal gravity waves?

a. Stage I—Primary mid- to upper-tropospheric wind adjustment

Isotachs of total and ageostrophic wind fields at 300 hPa from the UT simulation for 0400, 0800, and 1200

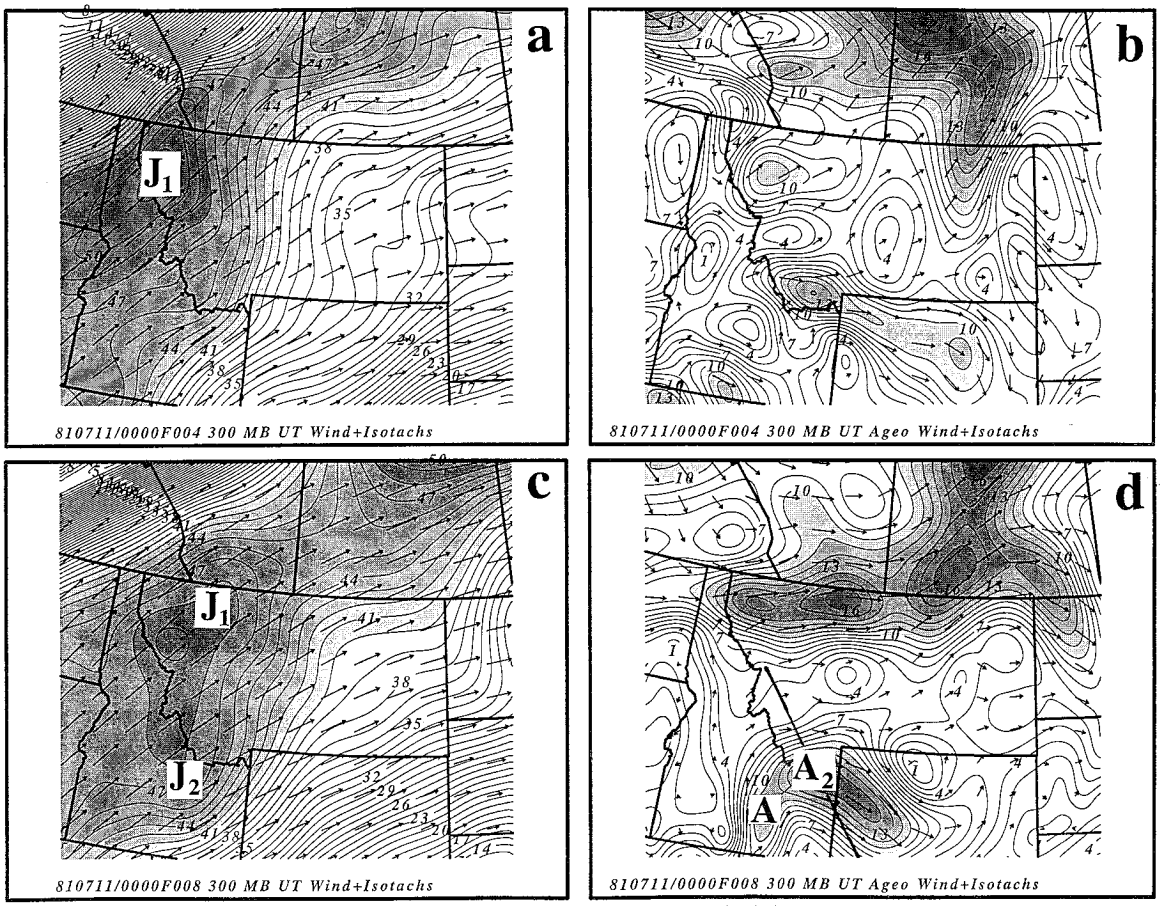

FIG. 10. The UT coarse mesh simulation of 300-hPa total wind vectors and isotachs (m s^{-1}) and ageostrophic wind vectors and isotachs (m s^{-1}) valid at (a),(b) 0400 UTC, (c),(d) 0800 UTC, (e),(f) 1200 UTC, and (g),(h) 1400 UTC 11 July 1981. Here, J_1 and J_2 represent mesoscale jet streaks (jetlets), while A and A_2 represent localized cross-stream ageostrophic wind maxima. Total (ageostrophic) wind speeds greater than or equal to 40 m s^{-1} (10 m s^{-1}) are shaded. Solid line in panel (d) indicates vertical cross section from Missoula, Montana (MSO), to just south of Big Piney, Wyoming (BPI), used in Fig. 13a.

UTC are depicted in Fig. 10. Since transient accelerations caused by mass-momentum adjustments during the first few (~3–4) hours of the model simulation are related to initialization procedures, we do not show fields prior to the 4-h forecast time. Two mesoscale jet streaks or ''jetlets'' appear over this period of time. The first jetlet (J_1), which propagates over western Montana, represents the downstream extension of the primary synoptic-scale jet exit region seen in the 0000 UTC 11 1981 July observations (Fig. 3). The second mesoscale jetlet (J_2) forms to the south-southwest of J_1 (just west of the WGR) by 0800 UTC, and continues to intensify thereafter.

Two mesoscale perturbations appear in the southeast to northwest height gradient in association with the two jetlets. These mass perturbations are manifested as geostrophic wind $\mathbf{V}_g$ maxima (Fig. 11b). One $\mathbf{V}_g$ maximum is located just northwest of the WGR. The westernmost $\mathbf{V}_g$ maximum over western Idaho reflects the larger-scale mass field supporting the primary jet streak. The dominant feature in the ageostrophic wind between 0400–0800 UTC (Figs. 10b and 10d) is a strong supergeostrophic region in southwestern Canada associated with the entrance region of a jet streak. However, of greater interest here is the localized ageostrophic wind maximum (A_2) that becomes increasingly southeastward-directed over the WGR (Fig. 10d). The advection of momentum in the right exit region of J_2 induces a substantial ageostrophic cross-contour flow v_{ag} toward higher heights, consistent with the deceleration of air parcels required under the quasigeostrophic system:

$$\frac{d_g u_g}{dt} = \frac{\partial u_g}{\partial t} + u_g \frac{\partial u_g}{\partial x} + v_g \frac{\partial u_g}{\partial y} = f v_{ag}. \qquad (1)$$

Clearly, quasigeostrophic theory is based on the use of the gradient of the geostrophic wind ($\mathbf{V}\cdot\nabla\mathbf{V}_g$), not the actual wind $\mathbf{V}\cdot\nabla\mathbf{V}$, in the inertial advective term. Yet, it is apparent that the rightward-directed cross-contour flow occurs in the exit region of the geostrophic jetlet, which is found over southwestern Idaho, as well (Figs. 11a and 11b). Therefore, these transverse circulations are consistent with the theory as applicable to straight

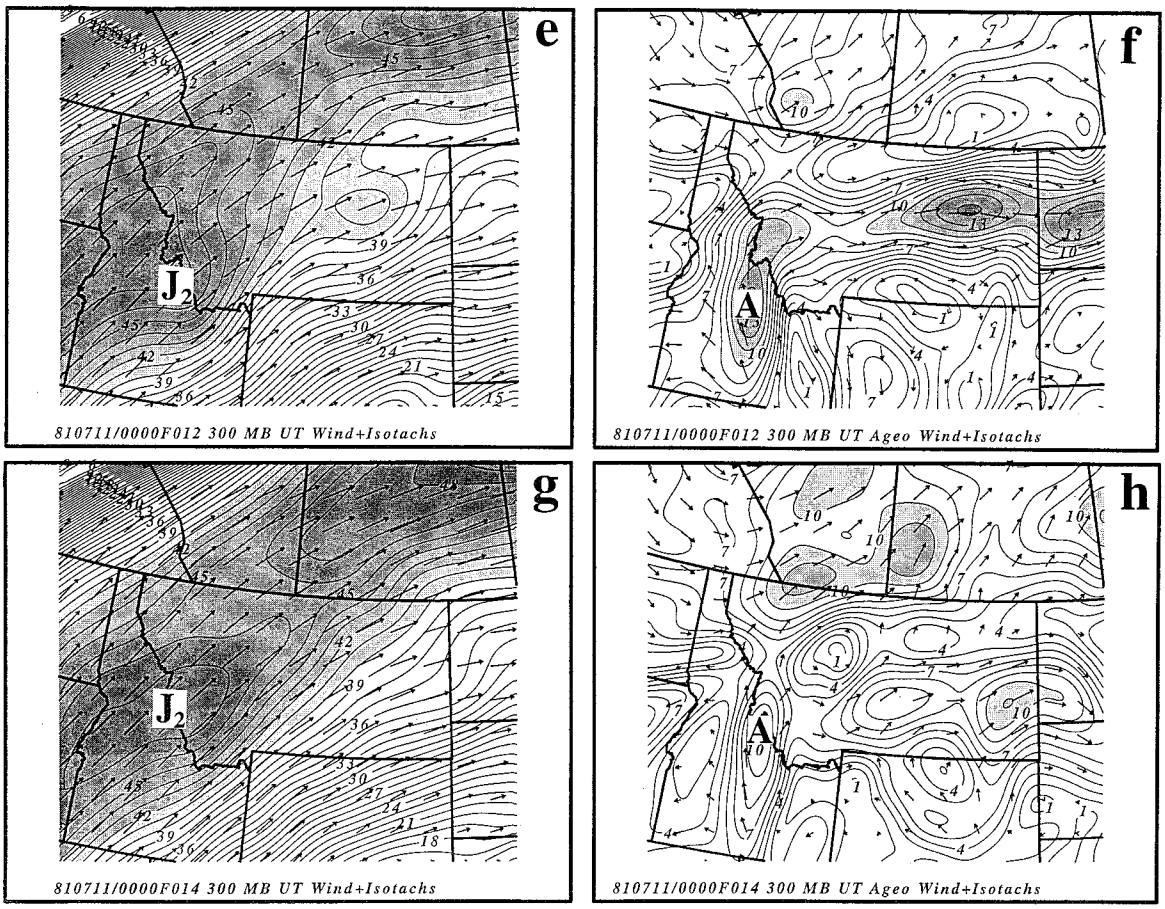

FIG. 10. (*Continued*)

jets, and thus are essentially balanced circulations between 0400 and 0800 UTC (e.g., Uccellini and Johnson 1979). Simultaneously, the entrance region of J_2 begins to develop a leftward-directed ageostrophic component by 0800 UTC over southeastern Idaho (A), which is directly upstream of the WGR. This important evolution marks the genesis of stage II.

b. Stage II—Primary mid- to upper-tropospheric mass adjustment and frontogenesis

The development of the leftward-directed ageostrophic flow (A) in the entrance region of J_2 and the embryonic geostrophic ''signal'' upstream of the WGR suggests that a new mass perturbation has developed almost simultaneously with J_2 just prior to 0800 UTC. This mass perturbation, which is frontogenetically forced, causes the air to accelerate within jetlet J_2's entrance region. Figure 12 depicts the 500-hPa height and temperature fields at 0200 and 0800 UTC as well as the total frontogenesis, and the tilting, confluence, and shear deformation terms in the frontogenesis equation at 0500 UTC, that is, during which time J_2 is forming. These frontogenesis forcing terms are computed from the following equation written in the model's sigma coordinates:

$$\frac{d}{dt}|\nabla\theta| = -\frac{1}{|\nabla\theta|}\left\{\underbrace{\left[\frac{\partial u}{\partial x}\left(\frac{\partial\theta}{\partial x}\right)^2 + \frac{\partial v}{\partial y}\left(\frac{\partial\theta}{\partial y}\right)^2\right]}_{\text{I}} + \underbrace{\left(\frac{\partial v}{\partial x}\frac{\partial\theta}{\partial x}\frac{\partial\theta}{\partial y} + \frac{\partial u}{\partial y}\frac{\partial\theta}{\partial x}\frac{\partial\theta}{\partial y}\right)}_{\text{II}} + \underbrace{\left(\frac{\partial\theta}{\partial x}\frac{\partial\dot{\sigma}}{\partial x}\frac{\partial\theta}{\partial\sigma} + \frac{\partial\theta}{\partial y}\frac{\partial\dot{\sigma}}{\partial y}\frac{\partial\theta}{\partial\sigma}\right)}_{\text{III}} + \frac{1}{c_p}\underbrace{\left(\frac{\partial\theta}{\partial x}\frac{\partial\dot{Q}}{\partial x} + \frac{\partial\theta}{\partial y}\frac{\partial\dot{Q}}{\partial y}\right)}_{\text{IV}}\right\} \quad (2)$$

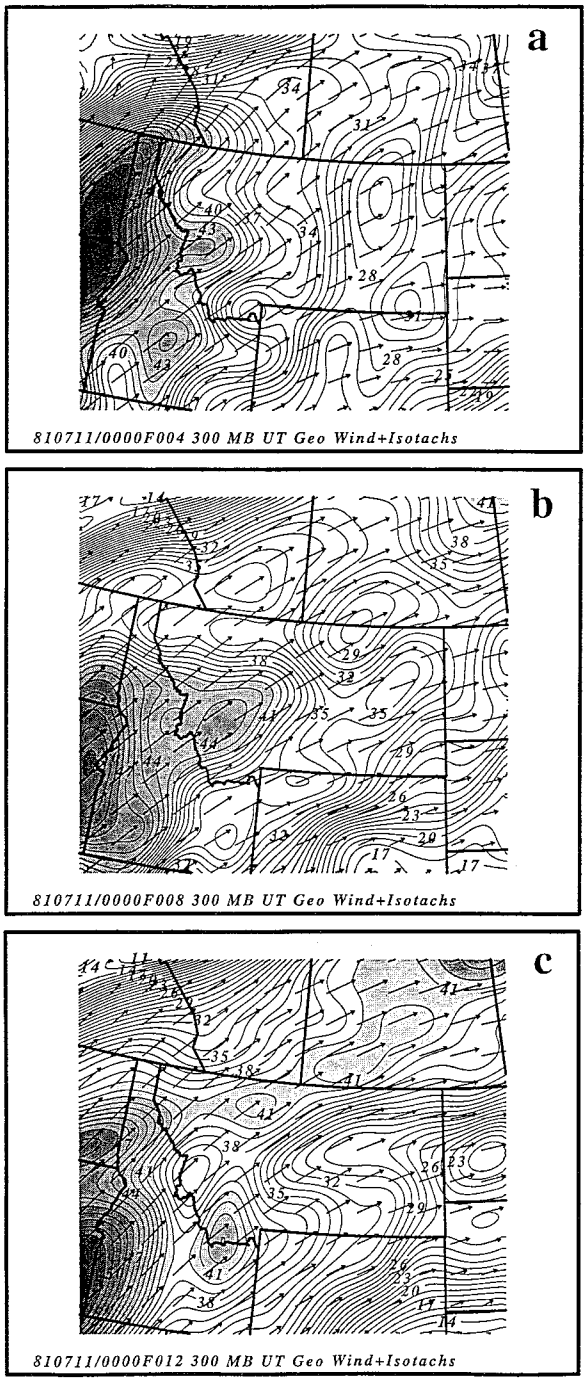

FIG. 11. The UT coarse mesh simulation of 300-hPa geostrophic wind vectors and isotachs (m s^{-1}) valid at (a) 0400 UTC, (b) 0800 UTC, and (c) 1200 UTC 11 July 1981. Geostrophic wind speeds greater than or equal to 40 m s^{-1} are shaded.

The respective terms in this equation are (I): confluence deformation acting upon the horizontal temperature gradient, (II) shearing deformation acting upon the horizontal temperature gradient, (III) tilting of horizontal isentropes into the vertical by the effects of differential vertical motion, and (IV) the frontogenetical forcing caused by horizontal gradients of diabatic heating. An inspection of the temperature fields at the two time periods as well as the total frontogenesis term reveals the development of a cross-stream frontal zone over the WGR. Shear and confluence deformation accompanying the development of J_2 are the primary processes responsible for the strong frontogenesis over the WGR. The shear is a reflection of the increasing inertial–advective processes accompanying J_1, which transport zonal kinetic energy into the region where J_2 forms between 0400 and 0800 UTC. Consistent with these processes, though of somewhat lesser magnitude, is the contribution from the tilting term, which is strongest over the northern part of the WGR. A strong cross-contour gradient in vertical motion exists here between the ascent over west-central Montana and the descent over northwestern Wyoming (Figs. 13a,b depict the ageostrophic secondary circulations about J_2). The diabatic differential heating (term IV) is negligible given the fact that no condensation is allowed in the simulation and that we are well above the planetary boundary layer during the evening time period (i.e., at 500 hPa at 1100 MDT).

These processes are consistent with jet streak circulations attempting to establish a balanced equilibrium. Accordingly, midtropospheric frontogenesis associated with the deceleration of air parcels in the exit region of J_2 occurs as the result of the thermally indirect circulation required to maintain thermal wind balance. Note that the maximum cooling over southwestern Montana and warming over northwestern Wyoming accompanying tilting motions about J_2 are shifted *well* to the southeast of J_1. This shift is due to the action of horizontal variations in vertical motion on the large vertical gradients of potential temperature within the middle troposphere over the WGR (Fig. 13a). The southeastward development of J_2 relative to J_1 is positioned above the strong cross-stream temperature gradient within the lower troposphere. This region of horizontal temperature gradient is just northwest of the very warm temperatures at 700 hPa over eastern Utah, southeastern Idaho, and northwestern Wyoming (Figs. 5c and 5d). As the thermally indirect ageostrophic circulation forms transverse to J_2 over the WGR, tilting of the isentropes into the horizontal plane occurs, thus accentuating the frontogenesis accompanying J_2. The resultant horizontal temperature gradient over the WGR is then acted upon by confluence (Fig. 12e) and shearing deformation (Fig. 12f). The resultant frontogenesis in the exit region of J_2 (Fig. 12c) is advected downstream over west-central Montana by 0800 UTC (Fig. 12b). This transverse secondary circulation is a highly transient feature of the evolving mesoscale flow. The mesoscale jetlet J_2 is not maintained long after this time, since the accompanying secondary circulation never achieves thermal wind balance required to maintain the jetlet, as explained next.

The pronounced spatial changes in the thermal wind

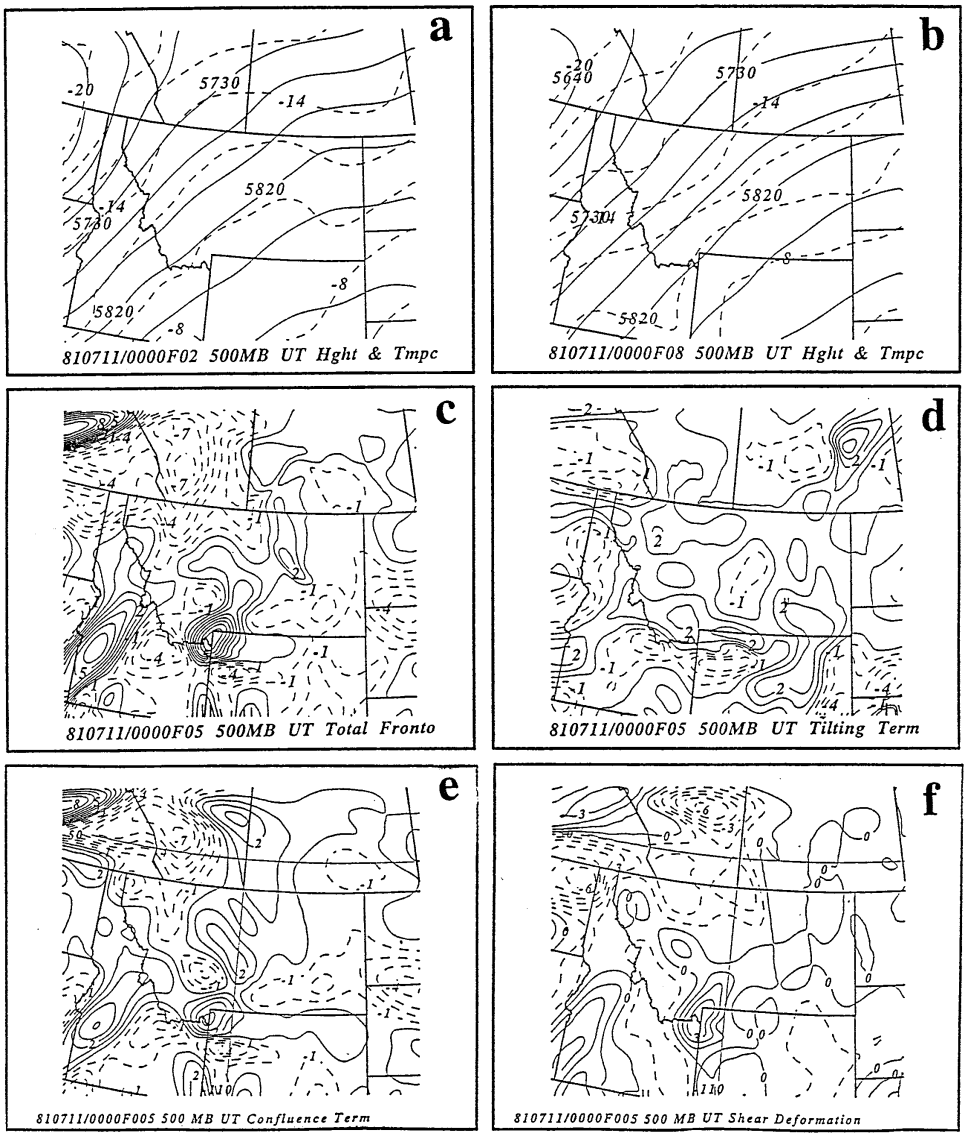

FIG. 12. The UT coarse mesh simulation of 500-hPa height (m) and temperature (°C) valid at (a) 0200 UTC and (b) 0800 UTC. Also shown are (c) total frontogenesis ($\times 10^9$ K m^{-1} s^{-1}) and (d)–(f) frontogenesis tilting, confluence, and shear deformation forcing terms ($\times 10^9$ K m^{-1} s^{-1}) respectively, valid at 0500 UTC 11 July 1981.

vector within the 300–500-hPa layer (Fig. 14a) across the WGR reflect a thermal wind imbalance associated with the strong rightward-directed ageostrophic flow A_2 (Fig. 10d). It is important to note that this southeastward-directed ageostrophic wind accompanying the thermally *indirect* circulation associated with J_2 (Figs. 13a,b) is actually located in the *entrance* region of the geostrophic jet (Fig. 11b), which comprises a portion of jetlet J_2. Therefore, it can be inferred that there may be a significant imbalance in the thermal wind accompanying the development of J_2. To more definitively address the thermal wind balance associated with the development of jetlet J_2, the computed thermal wind vectors in the 300–500-hPa layer were added to the model-simulated 500-hPa winds. This resulting vector wind was then subtracted from the model-simulated 300-hPa winds. Regions of significant nonzero vector winds therefore indicate areas of thermal wind imbalance, that is, unbalanced flow with respect to the thermal wind structure of the evolving flow. The results (Fig. 14b), which are similar to the ageostrophic winds (Figs. 10b and 10d), indicate that during this time period, significant thermal wind imbalance on the order of about 15 m s^{-1} exists near the WGR in northwestern Wyoming.

Consistent with this mass adjustment producing J_2 is the existence of the secondary jet streak inferred from satellite data over the WGR at 1200 UTC in Fig. 6.

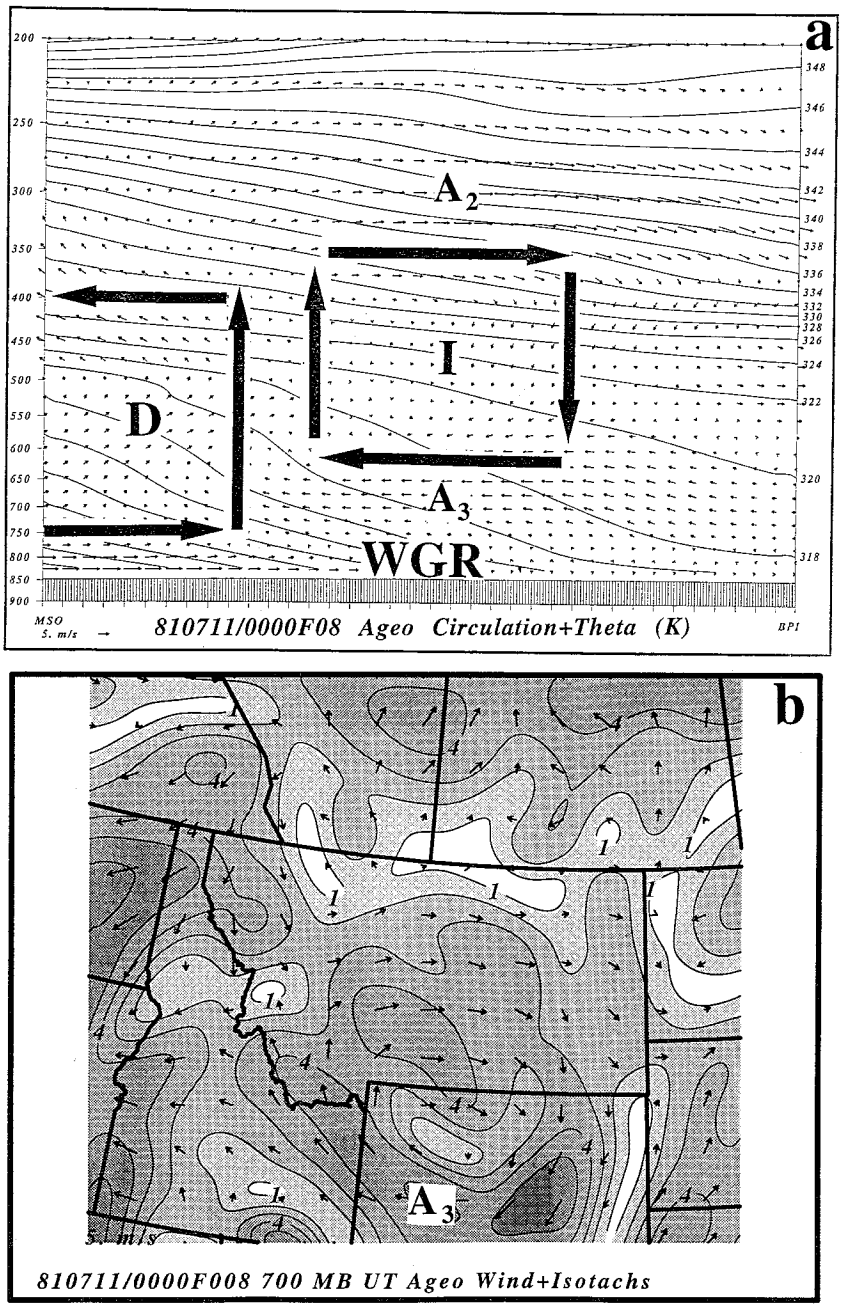

FIG. 13. (a) Ageostrophic circulation vectors and potential temperature (K) in the exit region of jetlet J_2 along the cross section from Missoula, Montana (MSO), to just south of Big Piney, Wyoming (BPI), depicted in Fig. 10c and valid at 0800 UTC 11 July 1981 from the UT coarse mesh simulation. Here, A_2 and A_3 represent, respectively, the upper- and lower-level return branch circulations accompanying J_2; ''I'' represents thermally indirect and ''D'' thermally direct circulations. (b) The UT coarse mesh 700-hPa ageostrophic wind vectors and isotachs ($\geq$1 m s^{-1} shaded) valid at 0800 UTC 11 July 1981. Here, A_3 represents the low-level return branch ageostrophic circulation accompanying the mid- to upper-tropospheric jetlet J_2.

Hence, the rightward-shifted cooling accompanying the circulation about J_2 depicted in Fig. 12 produces a mid- to upper-tropospheric companion geostrophic wind maximum.

To compare these adjustments with those of classical adjustment theory (e.g., Rossby 1938; Cahn 1945; Blumen 1972), we calculated the deformation radius, defined here following Frank (1983) as

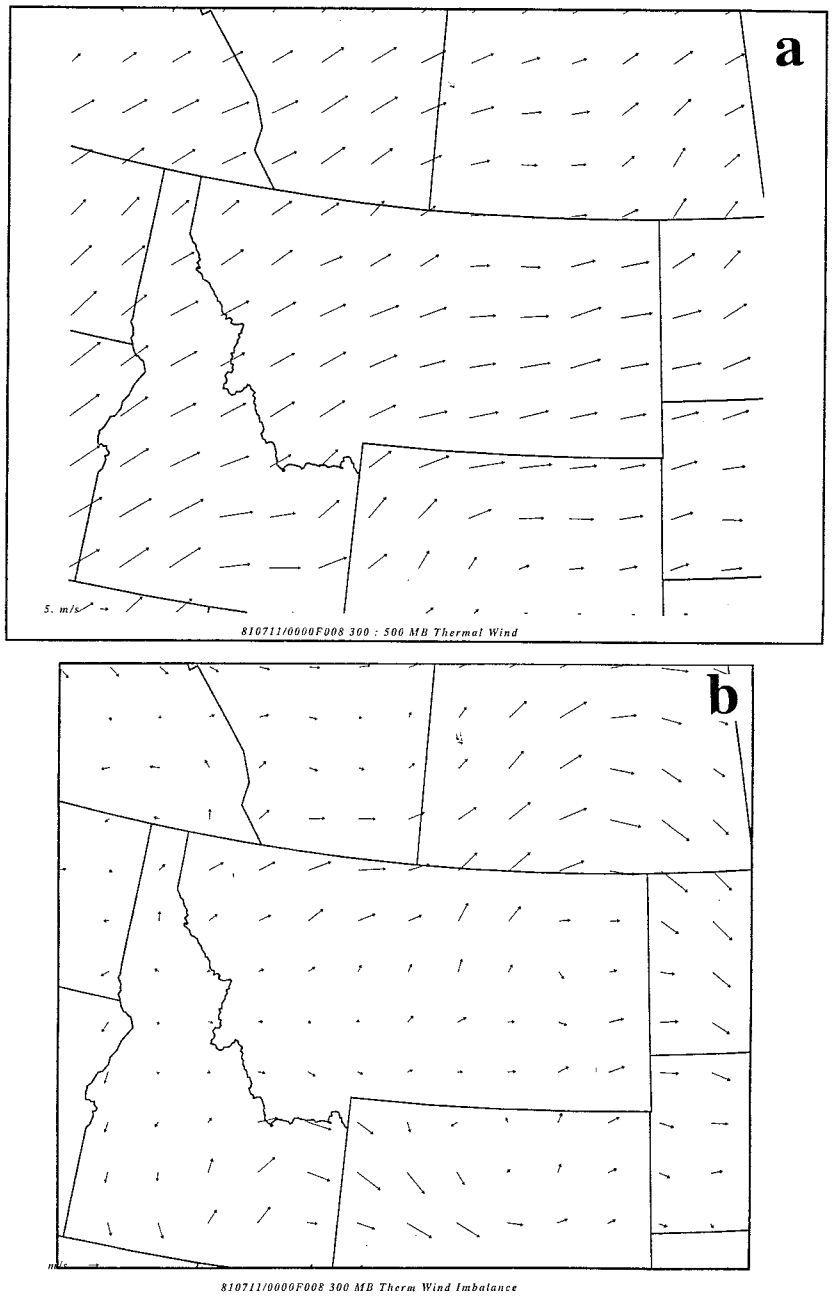

FIG. 14. The UT coarse mesh simulation of (a) thermal wind vectors and (b) thermal wind imbalance vectors valid at 0500 UTC 11 July 1981 for the layer between 500 and 300 hPa.

$$L_R = \frac{NH}{2\pi(\zeta + f)^{1/2}\zeta^{1/2}}, \tag{3}$$

where N is the layer-averaged Brunt–Väisälä frequency, H is the depth of the transverse circulation about J_2, ζ is the relative vorticity, and f is the Coriolis parameter. We estimate from Fig. 13 that $N \sim 0.007\ s^{-1}$, $H \sim 6$ km, and given that $f \sim 1.2 \times 10^{-4}\ s^{-1}$ and that over the WGR $|\zeta| \sim 2 \times 10^{-6}\ s^{-1}$ (the flow exhibits anti cyclonic curvature), we determine a deformation radius of about 435 km. From Figs. 10c and 10d, the horizontal scale of jetlet J_2 is approximately 250–300 km. Therefore, since $L_{J_2} \leq L_R$, classical adjustment theory predicts that the mass field should adjust to the disturbance (J_2) in the momentum field. This is manifested as the exit region frontogenesis accompanying the transverse circulation about J_2.

c. Stage III—Unbalanced adjustment occurring between J_2 and the primary polar jet

We have just seen how the restructuring of the exit region of the primary polar jet streak resulted in the development of J_1 and J_2 during the 0400–0800 UTC time period. The most important consequence of these adjustments has been to shift the mid- to upper-tropospheric baroclinic zone supporting the polar jet streak southeastward from northern Idaho at 0000 UTC into central and southwestern Montana by 0800 UTC (Figs. 12a,b). Hence, the development of jetlet J_2 has resulted in a set of conditions wherein the baroclinic zone in the exit region of the polar jet (the geostrophic jet core) is no longer colocated with the along-stream velocity gradient. Another way of understanding this is by observing that by 0800 UTC, the entrance region of jetlet J_2 over south central Idaho is becoming juxtaposed with the exit region of the geostrophic wind maximum associated with the primary polar jet located over extreme western Idaho (as depicted in Figs. 10c and 11b). Under these circumstances, the advection of geostrophic momentum by the total wind is not equal to the advection of total momentum by the total wind—that is, $\mathbf{V}\cdot\nabla\mathbf{V}_g \neq \mathbf{V}\cdot\nabla\mathbf{V}$—so the resulting ageostrophic cross-contour flow will be inconsistent with balanced concepts of upper-level jet–frontal systems. The development of J_2 effectively interferes with the balanced adjustment of the mass and momentum fields within the polar jet that had occurred in stage I. This unbalanced ageostrophic flow was also crudely detected in the observational analyses of Koch and Dorian (1988). The cross-stream ageostrophic flow (A) at 1200 UTC (Fig. 10f) is directed to the cyclonic side of the jet in the exit region of the geostrophic wind maximum. These dynamics are consistent with a flow in which *accelerations* occur within the exit region of a straight jet streak; hence, the exit region flow is no longer balanced (e.g., Kaplan and Paine 1977; Zack and Kaplan 1987; Uccellini and Koch 1987; Koch and Dorian 1988).

During the 0800–1200 UTC time period, the cross-stream height gradient just upstream of the WGR intensifies accompanying the earlier J_2 exit region frontogenesis, which creates a significant Laplacian of height over this region. This process occurs hydrostatically in conjunction with the tilting of isentropic surfaces into the horizontal plane within the 300–500-hPa layer, forming a significant horizontal temperature (height) gradient. These changes in the geopotential height field result in changes in the accompanying geostrophic winds. In particular, the area between the exit region of the geostrophic jet associated with J_1 over extreme western Idaho (Figs. 11b and 11c) and the entrance region of J_2 over south central Idaho (Fig. 10c) becomes progressively more subgeostrophic during the 0800–1200 UTC time period (Figs. 10d and 10f). As a consequence, conservation of momentum requires that a southerly ageostrophic flow develop in this region in order to restore thermal wind balance. This leftward-directed flow acts to minimize the existing rightward-directed thermal wind imbalance and persists in central Idaho through 1400 UTC (Figs. 10g–h).

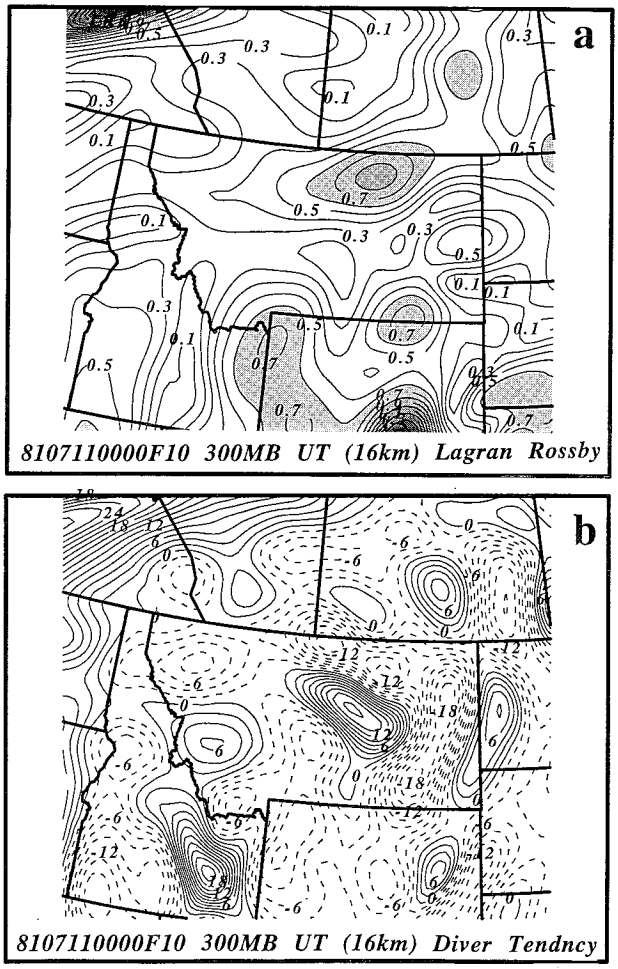

FIG. 15. The UT coarse mesh simulation of (a) Lagrangian Rossby number and (b) total horizontal wind velocity divergence tendency ($\times 10^9$ s^{-2}) valid at 1000 UTC 11 July 1981.

Another indicator of the degree of dynamical imbalance present over the WGR is the Lagrangian Rossby number (Ro). We computed Ro for comparison with the estimates from observations by Koch and Dorian (1988), and the Lagrangian divergence tendency fields. The Ro field was calculated as the ratio of the magnitude of the vector sum of the local plus inertial advective accelerations to the Coriolis acceleration:

$$\mathrm{Ro} = \frac{\left|\dfrac{\partial \mathbf{V}}{\partial t} + \mathbf{V}\cdot\nabla\mathbf{V}\right|}{|f\mathbf{V}|}. \tag{4}$$

This field is displayed in Fig. 15a, while the sum of the terms on the right side of the horizontal wind velocity divergence equation

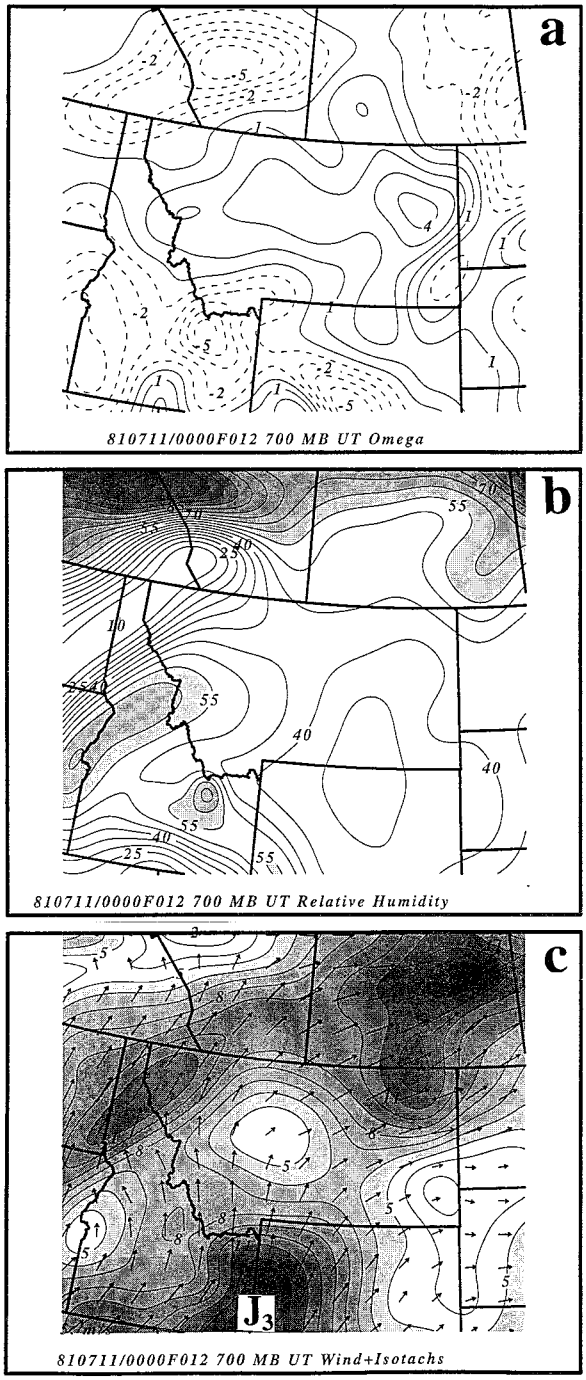

FIG. 16. The UT coarse mesh simulation of 700-hPa (a) vertical motion (μb s^{-1}), (b) relative humidity (%), and (c) wind vectors and isotachs (m s^{-1}) valid at 1200 UTC 11 July 1981. Here, J_3 represents the mesoscale midlevel jetlet. In panel (c) wind speeds greater than or equal to 5 m s^{-1} are shaded.

$$\frac{\partial D}{\partial t} + \mathbf{V}\cdot\nabla D + \omega\frac{\partial D}{\partial p} = D^2 - \left(\nabla\omega\cdot\frac{\partial \mathbf{V}}{\partial p}\right) + f\varsigma - \beta u + 2J(u, v) - \nabla^2\phi \qquad (5)$$

is displayed in Fig. 15b. The terms on the left side of (5) represent the local tendency of divergence D, and the horizontal and vertical advection of D, respectively. The six terms on the right side represent the nonlinear effect of divergence, the effect of vertical wind shear acting upon horizontal gradients of vertical motion, the relative vorticity effect, the β term (small), the Jacobian term (which is large in regions where horizontal wind shear and curvature are significant), and the Laplacian of the geopotential (which can be combined with the vorticity term to produce the ageostrophic vorticity). Large parcel divergence tendencies resulting from a significant nonzero sum of the terms on the right side of (5) will be reflected in terms of high spatial variability in the Lagrangian Rossby number field.

Kaplan and Paine (1977) showed that significant increases in upper-level divergence occur in regions that have large nonzero sums of the last four terms in (5), which together constitute the *nonlinear balance equation.* Zack and Kaplan (1987) found that this situation occurs where the Laplacian and Jacobian terms (the last two terms) are large and of like sign; however, these two terms are highly scale-dependent and will tend to dominate the other terms as the scale decreases (Kaplan and Paine 1977). Attempts to use mesoscale rawinsonde data to compute the terms of the nonlinear balance equation to diagnose the presence of unbalanced flow have been rare and fraught with sensitivity to random errors (Moore and Abeling 1988), whereas previous use of mesoscale models to evaluate the equation has not explored such possibilities with model grid resolutions less than 50 km. The results presented in the present paper constitute the first attempt to apply these diagnostic equations to high-resolution model datasets.

The results shown in Fig. 15 indicate the presence of moderately unbalanced flow conditions (Ro $>$ 0.7 and strong parcel divergence tendency) at and just upstream of the WGR, which is precisely the same area where unbalanced ageostrophic flow has developed between 0800 and 1200 UTC (Figs. 10 and 14). Although other maxima appear over eastern Wyoming and Montana, they are associated with considerably weaker wind speeds because these regions are removed from the jet streaks. For this reason, and the fact that only the unbalanced flow region near the WGR actually strengthens later in the model simulation (Fig. 10f), strongest emphasis should be placed on the unbalanced dynamics that are occurring there.

d. Stage IV—Development of the secondary midlevel jetlet over the WGR

The polar jet right exit region continued to remain centered just upstream of the WGR despite the many changes that have taken place to the jet and to its baroclinic support over the past 8–12 h. Since the original jet has bifurcated and reformed, the leftward-directed ageostrophic component of the polar jet exit region will

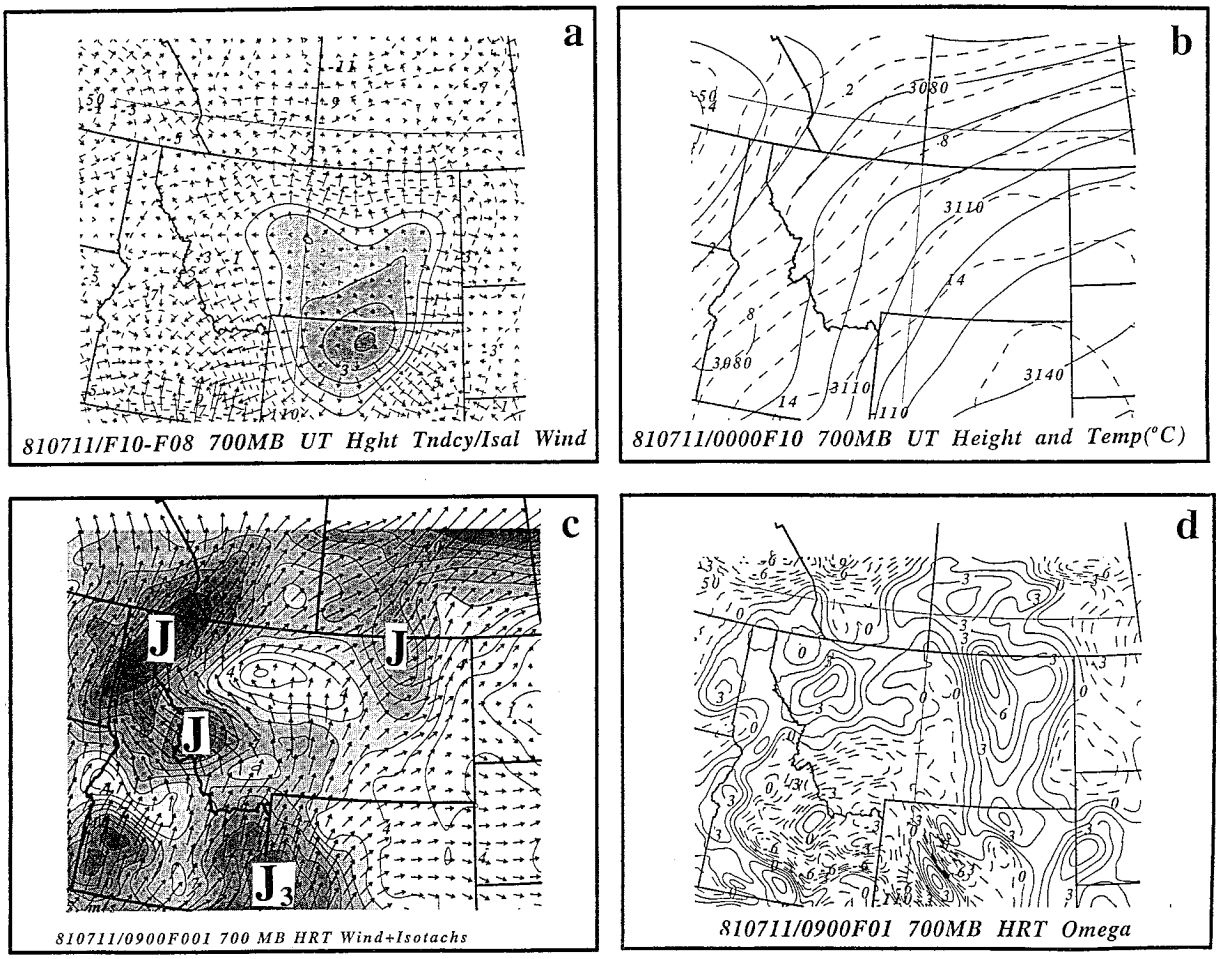

FIG. 17. The UT coarse mesh simulation of 700-hPa (a) geopotential height change (m) and isallobaric wind vectors (m s^{-1}) valid between 0800 UTC and 1000 UTC 11 July 1981 and (b) geopotential height (m) and temperature (°C) valid at 1000 UTC 11 July 1981. HRT nested-grid simulation of 700-hPa (c) wind vectors and isotachs (m s^{-1}) and (d) vertical motion (μb s^{-1}) valid at 1000 UTC 11 July 1981. In panel (c) J_3 represents the primary mesoscale midlevel jetlet, while J's indicate other mesoscale wind maxima.

be designated A in the remainder of this paper. Its location is over central Idaho by 1200 UTC (Fig. 10f), which is consistent with the observed location depicted in Fig. 7b and persists through 1400 UTC (Figs. 10g–h). The UT forecast 700-hPa winds, relative humidity, and vertical motion fields valid at 1200 UTC are depicted in Fig. 16. Several midlevel jetlets are present, but the most pronounced feature is jetlet J_3. This jetlet is intensifying over the WGR directly under the area where relatively unbalanced flow accompanying A was developing.

The reason for the development of J_3 can be seen in the 1000 UTC forecast fields from the nested-grid HRT simulation (Fig. 17). The 700-hPa trough that is propagating eastward across southern Idaho (Fig. 17b) reflects the increasing velocity divergence aloft accompanying the development of J_2's entrance region and A's leftward-directed ageostrophic flow. The velocity divergence accompanying these ageostrophic adjustments produces a nonuniform pressure fall field that distorts the 700-hPa height pattern, because as the height falls propagate southeastward to southern Idaho, an isallobaric convergence center develops during the 0800–1000 UTC time period (Fig. 17a). The low-level isallobaric acceleration acts to increase the southerly wind component in extreme southern Idaho and to turn the winds from southwesterly to south-southwesterly in western Wyoming (Fig. 17c). The combined effect of these isallobaric adjustments is to produce a mesoscale jetlet (J_3) that is directed toward the mountainous region of the WGR. In other words, A_3 represents the low-level return branch of the thermally indirect circulation accompanying J_2, but fortified by velocity divergence accompanying the entrance region of J_2 and the unbalanced adjustments that create velocity divergence accompanying A. Recall that the rawinsonde analyses depict this 700-hPa southwesterly jet extending from southern Idaho southward into Utah at 1200 UTC (Fig. 4f). The model results provide additional insight into the nature of this jetlet, since GMASS shows that J_3 is

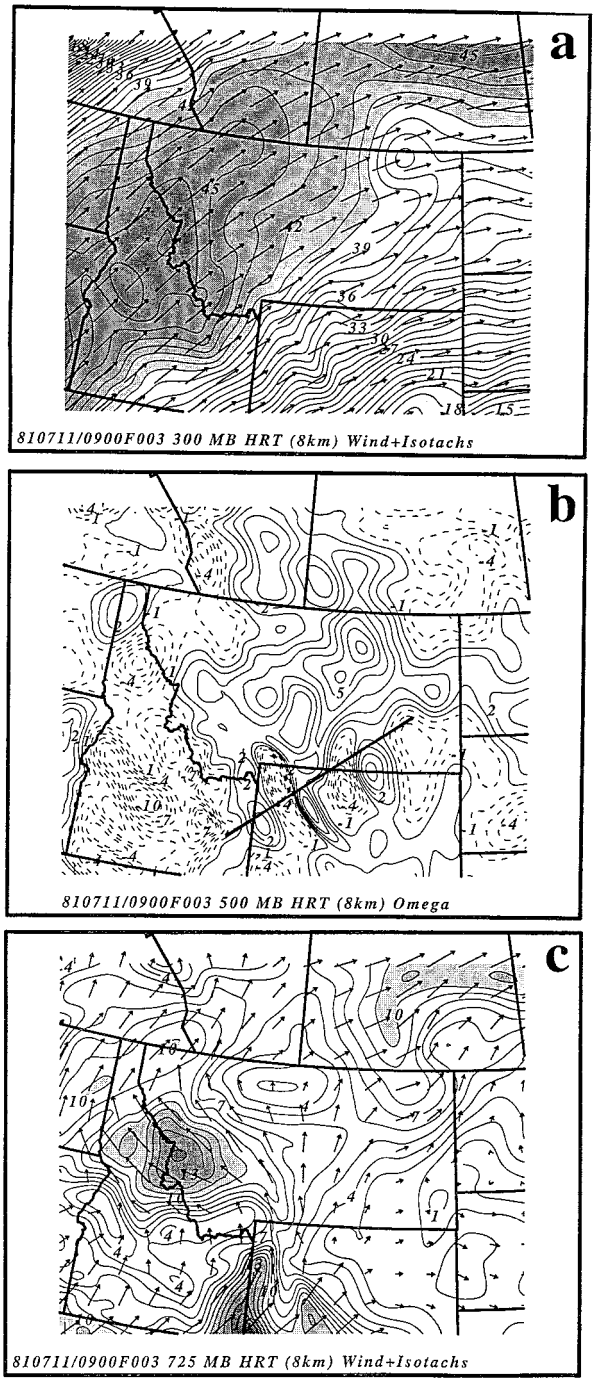

FIG. 18. HRT nested-grid simulation of (a) 300-hPa wind vectors and isotachs (m s^{-1}), (b) 500-hPa vertical motion (μb s^{-1}), and (c) 725-hPa wind vectors and isotachs (m s^{-1}) valid at 1200 UTC 11 July 1981. Solid line in panel (b) indicates vertical cross section from Malda, Idaho (MLD), to Miles City, Montana (MLS), used in Fig. 19.

not merely a southeastward shift of the 700-hPa wind maximum that was observed 12-h earlier over eastern Washington (Fig. 3f), but rather, it is generated locally by a complex sequence of geostrophic adjustment processes.

This new midlevel jetlet is accompanied by significant values of velocity convergence along its forward flank over the WGR. Thus, considerable ascent and moistening develop over the WGR by 1200 UTC at the 700-hPa level (Figs. 16a,b, 17d), and even as high as 300 hPa (not shown). Most importantly, this secondary ascent and relative humidity pattern occurs very close in space and time to the genesis of the first gravity wave episode observed by Koch and Golus (1988), and to the cirrus streak that forms over the WGR (Fig. 6). Also, the intensification of J_3 acts to reduce the 700-hPa warm pool responsible for the thermal wind imbalance by advecting it downstream away from the WGR.

e. Terrain-induced mass/momentum perturbations diagnosed from the LRT and HRT simulations

The UT simulation produces relatively broad vertical velocity fields (Fig. 16a) that do not display the northwest–southeast alignment consistent with the pressure change fields accompanying the gravity waves observed by Koch et al. (1988). Wavelengths as long as 700 km that are common in these vertical motion patterns are roughly four times larger than the observed 160-km primary wave modes. However, the LRT (not shown) and HRT simulations produce vertical motion patterns displaying a wavelength less than 200 km over the WGR (Fig. 18b). Notice that the waves are aligned orthogonal to the jet and parallel to the terrain axes. The orientation, position, and wavelength are very similar to the gravity waves observed by Koch et al. (1988) to have developed over the WGR beginning about 1100 UTC 11 July 1981.

The cross-terrain flow is best inferred from the simulated HRT wind field near the surface at 725 hPa (Fig. 18c). Vertical cross sections of isentropes, along-stream winds, and vertical motions are displayed in Fig. 19. As the midlevel jetlet J_3 starts to propagate toward the western side of the Absaroka Mountains in the nested-grid HRT simulation, there is little indication of terrain-induced vertical velocity perturbations until shortly before 1200 UTC, when the large-scale pattern of ascent over eastern Idaho and western Wyoming splits into two distinct waves with an average wavelength of about 200 km. The scale of these features is equivalent to the separation between the Absarokas and Big Horn Ranges in the plane of these cross sections (see also Fig. 2).

The mesoscale vertical velocity perturbations resulting from the interaction of the midlevel jetlet with the topographic features in the HRT simulation resemble quasistationary hydrostatic mountain waves, even insofar as the upstream tilt of the vertical motions is concerned, though the isentropic fields do not display the characteristic overturning until 1900 UTC (Fig. 19d). As expected, the HRT simulation produces a larger amplitude and shorter wavelength disturbance than the LRT simulation.

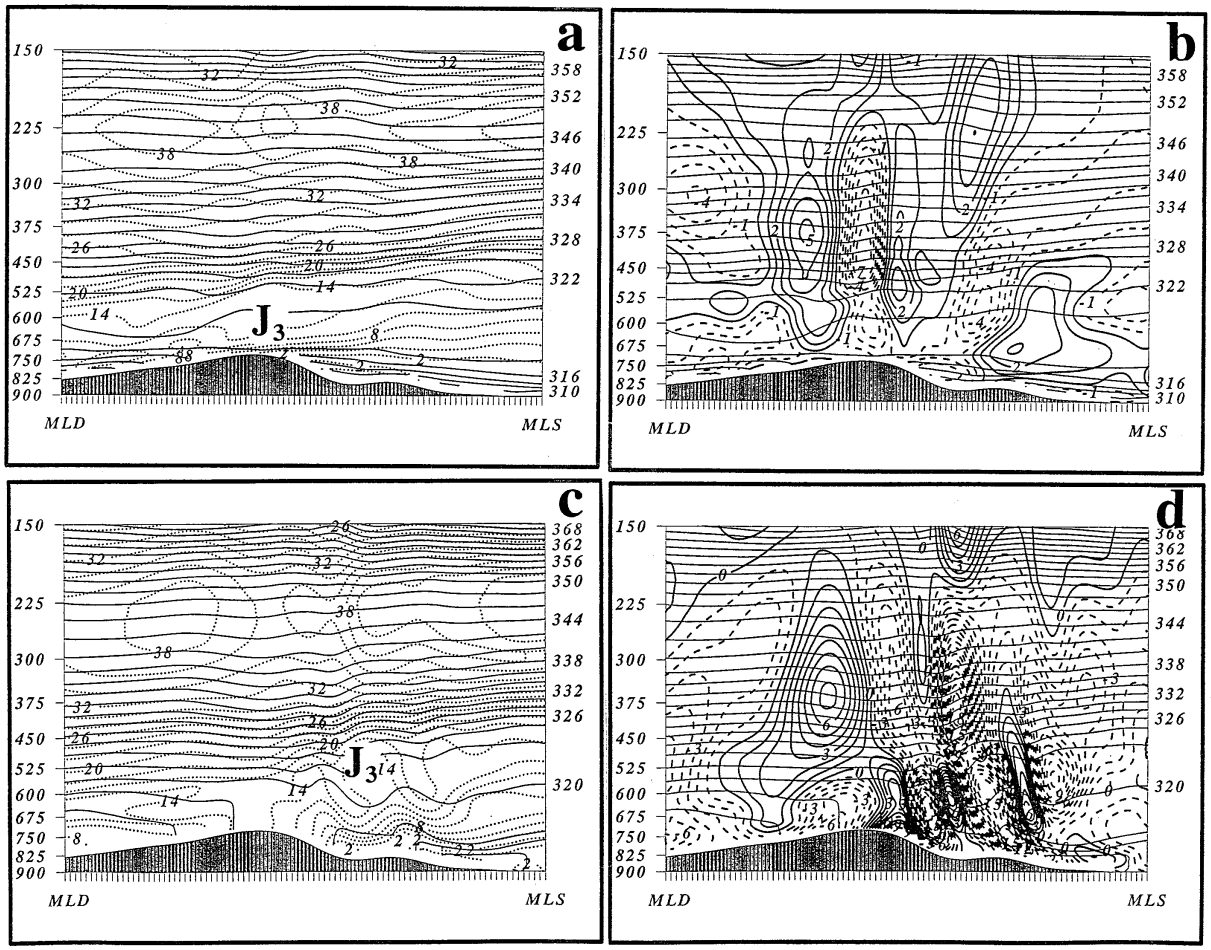

FIG. 19. HRT nested-grid simulation of vertical cross sections from Malda, Idaho (MLD), to Miles City, Montana (MLS), of potential temperature (K, solid) and wind velocity isotachs in plane of the cross section (m s^{-1}, dashed) as well as potential temperature (K, light solid) and omega (μb s^{-1}, solid—descent and dashed—ascent) valid at (a),(b) 1200 UTC and (c),(d) 1900 UTC 11 July 1981. Here, J_3 represents the primary mesoscale midlevel jetlet.

Although specifics of the gravity wave generation process will be examined in depth in a later paper to include idealized model experiments, we hypothesize that the terrain-induced mass perturbations in the exit region of J_3 produce along-stream variations in the pressure gradient force which, in turn, force large horizontal velocity divergence tendencies and parcel accelerations. These effects are seen in the 300-hPa unbalanced flow diagnostics depicted in Fig. 20 at 1200 UTC from the HRT nested-grid simulation. Hence, the effect of the along-stream height perturbations induced by terrain is to produce integrated velocity divergence tendencies that result in large tendencies in the mean sea level pressure. Although these mesoscale features in the pressure, wind, potential temperature, and vertical velocity fields have a wavelength of 150–200 km and are clearly absent in the UT nested-grid simulation, it takes several hours longer for these simulated mass and momentum perturbations to achieve the amplitude and even a portion of the phase velocity of those observed in nature by Koch and Golus (1988). The absence of a physical process or processes responsible for these deficiencies will be addressed in a future paper on wave generation mechanisms.

6. Summary and conclusions

In the first of a series of papers on the physical mechanisms responsible for the generation of the mesoscale gravity waves observed by Koch and Golus (1988), we have examined how geostrophic adjustment processes produced an ageostrophic mesoscale jet streak in the midtroposphere close to the location and time of observed wave generation. Mesoscale numerical simulations employing three different terrain configurations in which precipitation is totally suppressed all produce the mid- to low-level jetlet in approximately the same place and time. However, only the nested-grid simulations employing high-resolution terrain produce mesoscale waves in the mass and momentum fields with charac-

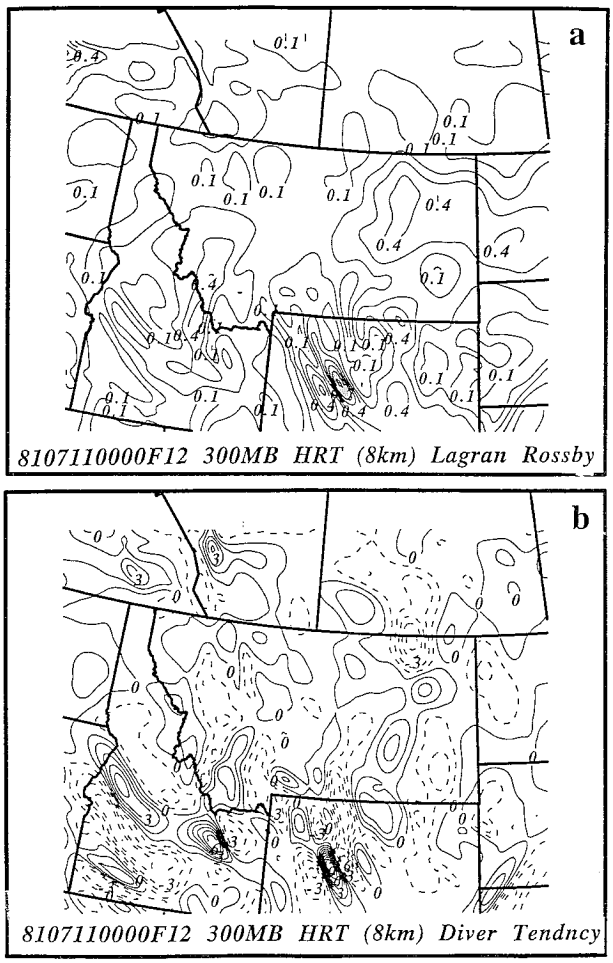

FIG. 20. HRT nested-grid simulation results at 300 hPa: (a) Lagrangian Rossby number calculated with 15-min interval datasets, and (b) total horizontal wind velocity divergence tendency valid at 1200 UTC 11 July 1981. In panel (a) Rossby number values greater than or equal to 0.5 are shaded.

teristic wavelengths analogous to the ''primary'' waves observed by Koch and Golus (1988). This indicates that 1) the background adiabatic geostrophic adjustment processes are responsible for midlevel jetlet formation independent of terrain, elevated sensible heating, or convective latent heating; 2) the location of the midlevel jetlet in close proximity to the orography is important in the wave generation process; and 3) the fine numerical resolution needed to resolve these approximate 150-km-wavelength features points toward nonlinear wave–wave interaction/amplification as critical to wave development. The simulations indicate that it is the perturbation of the midlevel mesoscale jetlet by the terrain-induced pressure ridges and troughs that results in mesoscale mass/momentum perturbations similar in many respects to the observed gravity waves. Therefore, it is very important to understand the role of geostrophic adjustment processes in mesoscale jetlet formation.

The four-stage sequence of events responsible for the development of the midlevel jetlet J_3 depicted in Fig. 21 involves both balanced and unbalanced adjustment processes. During stage I, a strong rightward-directed ageostrophic flow in the right exit region of the polar jet streak (J_1) is associated with a developing thermally indirect transverse circulation over west central Montana. This localized ageostrophic flow is the result of inertial-advective adjustments wherein air parcels decelerate as they pass through the exit region. As this balanced, thermally indirect, jet streak exit region circulation occurs northwest of the WGR, a separate mesoscale wind maximum (J_2) forms over the WGR in response to the inertial-advective forcing accompanying the ageostrophic circulation associated with J_1.

During stage II, J_2 intensifies as parcels accelerate within its entrance region. Midtropospheric frontogenesis occurs in the exit region of J_2 in response to the strong confluence, shearing deformation, and tilting accompanying the thermally indirect circulation there in the vicinity of the WGR. Stage II is complicated by the fact that substantial vertical gradients of potential temperature over the WGR modify the structure of the new front/transverse circulation as the isentropes are nonuniformly tilted into the horizontal plane. The vertical advection of potentially colder air during frontogenesis shifts the mass field accompanying J_2 downstream and to the right of the background larger-scale jet streak mass field. This shift ''detaches'' J_2 from J_1 and the larger-scale mass structure by virtue of the complex cooling and warming patterns.

Stage III involves a complex sequence of unbalanced adjustments. The development of J_2 forces the entrance region of this mesoscale jetlet to be juxtaposed with the geostrophic exit region of the primary polar jet. Thus, leftward-directed cross-contour ageostrophic flow develops between the polar jet exit region and J_2's entrance region. This results in the appearance of a new, highly unbalanced, localized, cross-stream ageostrophic wind maximum (A) because of the effect of geostrophic adjustment in accelerating the polar jet exit region, which happens to be situated over the WGR.

As the wind accelerates within the region of subgeostrophy between the geostrophic exit region of the polar jet and J_2's entrance region, vertically integrated velocity divergence develops, producing a mesoscale pressure perturbation within an advancing low pressure trough over southern Idaho. Mass flux divergence accompanying the velocity divergence tendencies within A produce surface pressure falls. This results in the onset of stage IV, wherein the low-level wind adjusts isallobarically to the new mesoscale mass field, by producing a midlevel jetlet (J_3). This jetlet becomes oriented orthogonal to the Absaroka and Big Horn mountain ranges. As the jetlet propagates over this orography, differential forcing due to adiabatic expansion and compression associated with developing hydrostatic mountain waves result in mass perturbations that eventually con-

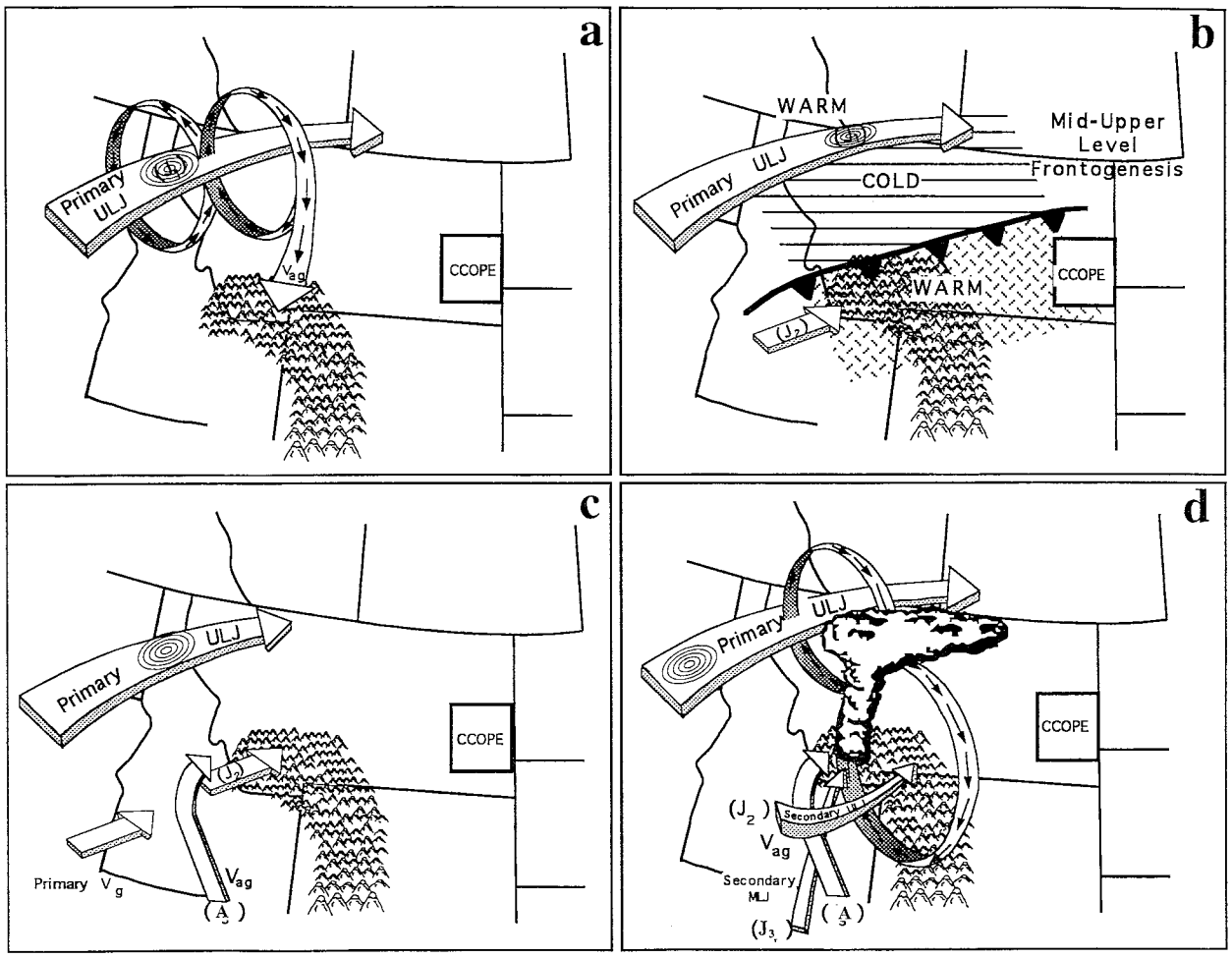

FIG. 21. Conceptual model deplicting the primary four-stage sequence of jet streak mass/momentum adjustments simulated to occur on 11–12 July 1981 in the vicinity of the WGR. (a) Stage I: alongstream inertial-advective processes result in a localized $\mathbf{V}_{ag}$ accompanying J_1. (b) Stage II: mid- to upper-level frontogenesis associated with the transverse ageostrophic circulation about J_1 produces mass perturbations resulting in J_2. (c) Stage III: Ageostrophic wind maximum (A) develops between the primary upper-level geostrophic jet exit region and the entrance region of J_2. (d) Stage IV: secondary midlevel jet streak J_3 (MLJ) develops in response to mass adjustments accompanying (A) and J_2. Arrows indicate the sense of the ageostrophic circulations about the meso-α- and meso-β-scale jet streaks (jetlets).

tract to a wavelength similar to that of the gravity waves observed during episode I of Koch and Golus (1988).

In summary, it is the nonlinear interaction between the midlevel jetlet (J_3) underneath the unbalanced flow aloft that excites and organizes the terrain-induced pressure perturbations, which eventually evolve into internal mass/momentum perturbations just downstream from the WGR. This interaction would be expected to occur between 500 and 700 hPa over the elevated terrain, as schematically depicted in Fig. 21, which is consistent with the findings of Koch et al. (1993). These investigators determined the wave source region—that is, the critical level—to be within this layer at about 5.5 km MSL. Additionally, it should be noted that the soundings from the CCOPE site at Knowlton, Montana, employed in their linear stability analyses were several hundreds of kilometers and more than 12 h after the episode I gravity wave event, which was observed to begin at approximately 1100 UTC 11 July 1981. Hence, the larger wind velocity at 1200 UTC 11 July 1981 between 500 hPa and 700 hPa may have resulted in a critical level lower than that calculated by Koch et al. (1993), thus adding credence to our conclusions that the layer between the middle and lower troposphere was key to gravity wave generation.

A second paper will examine the dynamics responsible for wave episode II, when elevated sensible heating in the planetary boundary layer produces a mountain–plains solenoid circulation in the GMASS model simulations, resulting in the modification of the mesoscale jetlets and internal gravity waves. Subsequent papers will also explore if and how convective latent heating and wave ducting modifies the numerically simulated internal gravity waves.

Acknowledgments. This work was funded under

NASA Contract NAG5-1790-21, United States Air Force Grant F49620-95-1-0226, and NSF Grant ATM-9319345. The authors wish to acknowledge Dr. Ramesh Kakar at NASA Headquarters and Dr. James Kroll at the USAF Office of Scientific Research for their support. We also thank Mr. David Hamilton, Mr. Michael Trexler, and Mr. Danny Felton for providing some of the GEMPAK shell scripts used in, and assistance with, figure preparation. Heather Bowden graciously donated her time and efforts in finalizing the drafts of several of the figures. Dr. Ahmet Aksakal formerly of NASA/GSFC and Dr. John Manobianco of ENSCO, Inc., as well as Drs. John Zack and Kenneth Waight III of MESO, Inc. provided assistance with model implementation and data ingestion. The computer time was provided by the North Carolina Supercomputer Center of the Microelectronics Center of North Carolina. Postprocessing of the model datasets was performed on the NCSC Cray Y-MP/E, and on the IBM-funded workstations of the North Carolina State University Facility for Ocean–Atmosphere Modeling and Visualization (FOAM^{V}).

REFERENCES

Blumen, W., 1972: Geostrophic adjustment. *Rev. Geophys. Space Phys.,* **10,** 485–528.

Cahn, A., 1945: An investigation of the free oscillations of a simple current system. *J. Meteor.*, **2,** 113–119.

Durran, D. R., and D. B. Weber, 1988: An investigation of the poleward edges of cirrus clouds associated with midlatitude jet streams. *Mon. Wea. Rev.,* **116,** 702–714.

Frank, W. M., 1983: The cumulus parameterization problem. *Mon. Wea. Rev.,* **111,** 1859–1871.

Fritsch, J. M., and C. F. Chappell, 1980: Numerical prediction of convectively-driven mesoscale pressure systems. Part I: Convective parameterization. *J. Atmos. Sci.,* **37,** 1722–1733.

Kaplan, M. L., and D. A. Paine, 1977: The observed divergence of the horizontal velocity field and pressure gradient force at the mesoscale. Its implications for the parameterization of three-dimensional momentum transport in synoptic-scale numerical models. *Beitr. Phys. Atmos.,* **50,** 321–330.

——, and V. M. Karyampudi, 1992a: Meso-beta scale numerical simulations of terrain drag-induced along-stream circulations. Part I: Midtropospheric frontogenesis. *Meteor. Atmos. Phys.,* **49,** 133–156.

——, and ——, 1992b: Meso-beta scale numerical simulations of terrain drag-induced along-stream circulations. Part II: Concentration of potential vorticity within dryline bulges. *Meteor. Atmos. Phys.,* **49,** 157–185.

——, J. W. Zack, V. C. Wong, and J. J. Tuccillo, 1982: Initial results from a mesoscale atmospheric simulation system and comparisons with the AVE-SESAME I data set. *Mon. Wea. Rev.,* **110,** 1564–1590.

Keyser, D., and M. A. Shapiro, 1986: A review of the structure and dynamics of upper-level frontal zones. *Mon. Wea. Rev.,* **114,** 452–499.

Koch, S. E., 1985: Ability of a regional scale model to predict the genesis of intense mesoscale convective systems. *Mon. Wea. Rev.,* **113,** 1693–1713.

——, and P. B. Dorian, 1988: A mesoscale gravity wave event observed over CCOPE. Part III: Wave environment and probable source mechanisms. *Mon. Wea. Rev.,* **116,** 2570–2592.

——, and R. E. Golus, 1988: A mesoscale gravity wave event observed during CCOPE. Part I: Multiscale statistical analyses of wave characteristics. *Mon. Wea. Rev.,* **116,** 2527–2544.

——, W. C. Skillman, P. J. Kocin, P. J. Wetzel, K. F. Brill, D. A. Keyser, and M. C. McCumbaer, 1985: Synoptic scale forecast skill and systematic errors in the MASS 2.0 model. *Mon. Wea. Rev.,* **113,** 1714–1737.

——, R. E. Golus, and P. B. Dorian, 1988: A mesoscale gravity wave event observed over CCOPE. Part II: Interactions between mesoscale convective systems and the antecedent waves. *Mon. Wea. Rev.,* **116,** 2545–2569.

——, F. Einaudi, P. B. Dorian, S. Lang, and G. M. Heymsfield, 1993: A mesoscale gravity wave event observed during CCOPE. Part IV: Stability analysis and Doppler-derived wave vertical structure. *Mon. Wea. Rev.,* **121,** 2483–2510.

Manobianco, J., L. W. Uccellini, K. F. Brill, and P. J. Kocin, 1991: Contrasting the impact of dynamic data assimilation on the numerical simulation of cyclogenesis during GALE IOP 10 and IOP 1. *Meteor. Atmos. Phys.,* **45,** 41–63.

——, ——, ——, and Y.-H. Kuo, 1992: The impact of dynamic data assimilation on the numerical simulation of the *QE II* cyclone and an analysis of the jet streak influencing the precyclogenetic environment. *Mon. Wea. Rev.,* **120,** 1973–1996.

——, S. E. Koch, V. M. Karyampudi, and A. J. Negri, 1994: The impact of assimilating satellite-derived precipitation rates on numerical simulations of the ERICA IOP 4 cyclone. *Mon. Wea. Rev.,* **122,** 341–365.

Molinari, J., 1982: A method for calculating the effects of deep cumulus convection in numerical models. *Mon. Wea. Rev.,* **110,** 1527–1534.

Moore, J. T., and W. A. Abeling, 1988: A diagnosis of unbalanced flow in upper levels during the AVE-SESAME I period. *Mon. Wea. Rev.,* **116,** 2425–2436.

Phillips, N. A., 1957: A coordinate system having some special advantages for numerical forecasting. *J. Meteor.,* **14,** 184–185.

Powers, J. G., and R. J. Reed, 1993: Numerical simulation of the large-amplitude mesoscale gravity wave event of 15 December 1987 in the central United States. *Mon. Wea. Rev.,* **121,** 2285–2308.

Rossby, C. G., 1938: On the mutual adjustment of pressure and velocity distributions in simple current systems, 2. *J. Mar. Res.,* **1,** 239–263.

Schmidt, J. M., and W. R. Cotton, 1990: Interactions between upper and lower tropospheric gravity waves on squall line structure and maintenance. *J. Atmos. Sci.,* **47,** 1205–1222.

Schneider, R. S., 1990: Large-amplitude gravity wave disturbances within the intense midwest extratropical cyclone of 15 December 1987. *Wea. Forecasting,* **5,** 533–558.

Tripoli, G. J., and W. R. Cotton, 1989: Numerical study of an observed orogenic mesoscale convective system. Part I: Simulated genesis and comparison with observations. *Mon. Wea. Rev.,* **117,** 273–304.

Uccellini, L. W., and D. R. Johnson, 1979: The coupling of upper- and lower-tropospheric jet streaks and implications for the development of severe convective storms. *Mon. Wea. Rev.,* **107,** 662–673.

——, and S. E. Koch, 1987: The synoptic setting and possible energy sources for mesoscale wave disturbances. *Mon. Wea. Rev.,* **115,** 721–729.

Whitaker, J. S., L. W. Uccellini, and K. F. Brill, 1988: A model-based diagnostic study of the rapid development phase of the Presidents' Day cyclone. *Mon. Wea. Rev.,* **116,** 2337–2365.

Zack, J. W., and M. L. Kaplan, 1987: Numerical simulations of the subsynoptic features associated with the AVE-SESAME I case. Part I: The preconvective environment. *Mon. Wea. Rev.,* **115,** 2367–2393.

Zhang, D.-L., and R. A. Anthes, 1982: A high resolution model of the planetary boundary layer—Sensitivity tests and comparisons with SESAME-79 data. *J. Appl. Meteor.,* **21,** 1594–1609.

——, and J. M. Fritsch, 1988: Numerical simulation of the meso-beta scale structure and evolution of the 1977 Johnstown flood. Part III: Internal gravity waves and the squall line. *J. Atmos. Sci.,* **45,** 1252–1268.